DEVELOPMENT AND COMMISSIONING OF A PHOTON DETECTION SYSTEM FOR COLLINEAR LASER SPECTROSCOPY AT NSCL

By

Sophia Vinnikova

A THESIS

Submitted to
Michigan State University
in partial fulfillment of the requirements
for the degree of

Masters of Science

Chemistry

2011

ABSTRACT

DEVELOPMENT AND COMMISSIONING OF A PHOTON DETECTION SYSTEM FOR COLLINEAR LASER SPECTROSCOPY AT NSCL

By

Sophia Vinnikova

A photon detection system has been developed for collinear laser spectroscopy measurements at the Beam COoling and COllinear LAser spectroscopy (BECOLA) facility at NSCL. The system is based on a design from the University of Mainz, and relies on an ellipsoidal reflector to transport fluorescent light to a photomultiplier tube. "Blue" and "red" photon detection systems were designed to cover the desired wavelength ranges. Simulations of the detection system were performed using FRED optical engineering software, and commissioning measurements were carried out with a 15 keV Ca^+ beam to evaluate performance and to optimize the"blue" photon detection system for the BECOLA facility. Signal to noise measurements with different arrangements of beamline apertures showed that apertures are necessary both upstream and downstream of the reflector to reduce scattered laser light. Signal to noise ratio measurements for various iris sizes at the second focal plane of the reflector showed that the signal to noise ratio increased with iris area less than 12.7 mm in diameter, and then saturated with increasing size. The signal distribution was found to peak at the second focal point of the ellipsoidal reflector, which was well reproduced by the simulations. The background distribution was uniformly distributed over the area of the second focal plane that was measured. Overall sensitivity of 1 photon per 128 ions was achieved with the present "blue" photon detection system.

ACKNOWLEDGMENTS

This thesis could not have been completed without the help of Photon Engineering, who gave me two years of gratis licences for FRED.

This thesis was also made possible with the help of many people. I would like to thank my adviser, Paul Mantica for the never ending questions during group meeting, for teaching me how to give presentations, and for the knowledge that he imparted onto me over the past two and a half years. Secondly I am eternally grateful to the BECOLA group, thank you Kei Minamisono, Andrew Klose and Anthony Schneider for the long days (and nights) spent in the experimental area as we searched for a resonance and for the even longer hours spent on my measurements after the resonance was observed. Additionally I want to thank Kei for letting me bounce ideas off him during the simulation and design processes.

I want to also thank my collaborators from the University of Mainz, especially Michael Hammen and Jörg Krämer for answering all of my questions about their photon detection systems.

Finally, I want to thank my friends and family for sticking by me, especially during the past semester. Thank you Mamma, Pappa, Asia and Inessa for the weekly skype calls, they brightened up my saturdays and got me out of bed before noon. Thank you Merle, Louisa, Ashley, and Jenn for the support and friendship that you have given me over the years. Also I want to give thanks to Atos and Konty, whose unconditional love always made the long drives home worth it.

Contents

List of Tables

List of Figures

Chapter 1

Introduction

1.1 Motivation

The main objectives of the BEam COoler and COllinear LAser spectroscopy (BECOLA) facility at the National Superconducting Cyclotron Laboratory (NSCL) are two-fold: (1) to measure hyperfine atomic structure of rare isotopes in order to deduce nuclear properties such as the electric quadrupole moment, the magnetic dipole moment, ground state nuclear spin, and the change in nuclear charge radius, and (2) to produce polarized nuclei for fundamental symmetry studies.

The hyperfine structure of an atom can be measured using atomic spectroscopy, where the absorption or emission of energy induces transitions between electronic states. The frequencies of photons absorbed or emitted is related to the difference in energy of the initial and final electronic states. Atomic fluorescence typically occurs with relatively little time delay; therefore the system needed to detect photoemission must be well matched to the source of the photons. The observed fluorescence is typically at the same frequency as the frequency used to induce the transition, for atomic spectroscopy. A photon detection system must be able to observe the fluorescence in the presence of a potentially large background. Most atomic spectroscopy experiments use lasers to induce the electronic excitations. Lasers have the advantages of

high power, continuous wave or pulsed operation, tunability, and a very collimated beam.

Lasers have been applied to hyperfine structure measurements of unstable isotopes for some 30 years. The most widely-applied technique is collinear laser spectroscopy. Such laser spectroscopy experiments have typically been performed at Isotope Separator Online (ISOL) type facilities, where the ion/atom beam is chemically extracted from the target due to strict requirements on the ion-beam [1]. Chemical extraction is difficult for some elements, such as transition metals, due to their high melting points.

The BECOLA facility will make use of isotopes produced by projectile fragmentation at National Superconducting Cyclotron Laboratory (NSCL). Projectile fragmentation coupled with in-flight separation is a "chemistry independent" method for isotope production that, coupled to beam thermalization, promises to extend the number of elements available for study by laser spectroscopy. NSCL has pioneered the thermalization of projectile fragments in helium buffer gas to produce high-quality, low-energy beams [2]. The BECOLA system will be placed downstream of the NSCL gas stopping area, and the low-energy beams will be available for a wide range of chemical elements to open new opportunities for laser spectroscopy studies [3]. Experiments with short-lived transition metals and other rare isotopes than have not been produced at other facilities [3] will be possible.

A key component of BECOLA is the fluorescent photon counting system, that was designed to meet the following requirements: (1) compatibility with a collinear geometry of the ion and laser beams; (2) efficient collection of fluorescent light, while blocking out stray light; (3) applicability over the wavelength ranges available from the existing BECOLA laser system; (4) ability to physically fit into the existing 8 inch diameter 6-way cross; and (5) applicability to both ion and atom beams.

This thesis describes the development of the photon detection system for blue light at BECOLA. The remainder of this chapter will provide background information on

collinear laser spectroscopy and on the experimental set-up at NSCL. The remaining chapters will discuss in detail the photon detection system model, design, fabrication, and commissioning tests.

1.2 Atomic Spectroscopy

Spectroscopy is the study of the absorbed or emitted energy to identify the transitions between states of a quantum mechanical system. Atomic spectroscopy generally deals with transitions among the electronic states of an atom. The frequency (ν) at which energy is absorbed or emitted is related to the difference in the energies of levels of the initial and final states. In the absence of recoil corrections, the energy difference between levels, ΔE, is given by:

$$\Delta E = h\nu = |E_2 - E_1| \tag{1.1}$$

where E_2 and E_1 are the energies of the final and initial states, respectively, and h is Plank's constant.

Atomic states of one electron systems can be described by the quantum numbers of that electron $nljm_j$, where n is the principal quantum number, l is the orbital angular momentum quantum number, j is the total angular momentum [with spin-orbit coupling where $j = l + s = l \pm \frac{1}{2}$, with s being the spin of the electron ($\pm\frac{1}{2}$)], and m_j is the projection of j onto the quantization axis. Electrons with the same n belong to the same shell, and electrons with the same n and j belong to the same subshell.

In many-electron systems, the angular momenta of the electrons have to be combined. In the LS coupling scheme, the total angular momentum, L, and the total electron spin, S, come from the coupling of the orbital angular momenta ($L = \sum_i l_i$) to the total angular momentum and spins of the electrons are coupled to a total electron spin ($S = \sum_i s_i$) respectively. Total spin J comes from the spin-orbit coupling

between S and L ($J = L + S$). Selection rules for allowed electric dipole (E1) transitions are: $\Delta l = \pm 1$, $\Delta L = 0, \pm 1$, $\Delta J = 0, \pm 1$, and $\Delta S = 0$. Δl is the change in the angular momentum of the electron undergoing the transition, and it must change by one because the photon carries one unit of angular momentum.

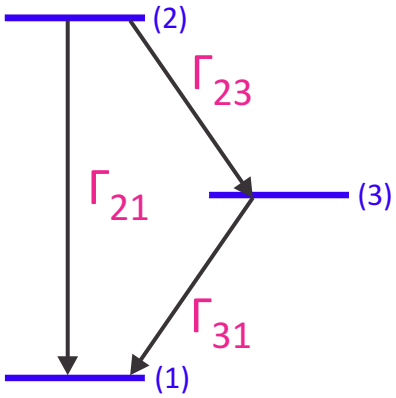

Figure 1.1: A three-level energy diagram. Possible transitions from the highest level are depicted by solid arrows. For interpretation of the references to color in this and all other figures, the reader is referred to the electronic version of this thesis.

As a simple example, a three-level energy diagram with an excited state, ground state, and intermediate state, denoted as (1), (2), and (3), respectively, is depicted in Fig. 1.1. The decay rates between electronic states are denoted by Γ_{ul} and are shown by the solid arrows. The total decay rate from state (2), Γ_2, needs to account for the decay rates of all possible paths from (2), and is related to the lifetime (τ) of level (2) and the natural line width $\Delta\nu_{nat}$ by the expression :

$$\Gamma_2 = \Gamma_{21} + \Gamma_{23} = \frac{1}{\tau_2} = 2\pi\Delta\nu_{nat}. \tag{1.2}$$

Eq. 1.2 can be rearranged to solve for the natural linewidth [4];

$$\Delta\nu_{nat} = \frac{1}{2\pi\tau} \tag{1.3}$$

The observed line shape for the fluorescence at frequency ν for an induced resonance frequency ν_0 is a Lorentzian profile with a full width at half maximum (FWHM)

of the natural linewidth, and a centroid of ν_0 [4]. The observed linewidth of a transition is generally broader than the natural linewidth; as a result of various experimental broadening effects attributed to the velocity distribution of the ion/atom beam as discussed below.

1.2.1 Line Broadening

The two main types of line broadening are labeled homogeneous and inhomogeneous. Homogeneous line broadening occurs with an ensemble of atoms with uniform response [5, 6]. Inhomogeneous broadening comes from the transition frequencies in a set of atoms with non-uniform response.

Doppler broadening is an example of inhomogeneous broadening caused by the Doppler effect on an ensemble of atoms moving with a random distribution of thermal velocities [5]. The line shape of inhomogeneous broadening gives a Gaussian line shape [5, 6].

Time-transit broadening due to the finite lifetime of the transition and power broadening due to saturation of the transition are examples of homogeneous line broadening, which gives a Lorentzian line shape [4, 7].

The experimentally-observed transition line shape can be modeled by a Voigt function, or Voigt profile, which is a convolution of a Gaussian with a Lorentzian. The linewidths of the Gaussian and Lorentzian components in the Voigt profile permit a quantitative means to deduce the contributions to the line shape due to homogeneous and inhomogeneous broadening [5]. The differences in line shape of Lorentzian, Gaussian, and Voigt profiles are depicted in Fig. 1.2. Notice that the Lorentzian function is more sharply peaked but yet is wider at the base than the Gaussian function.

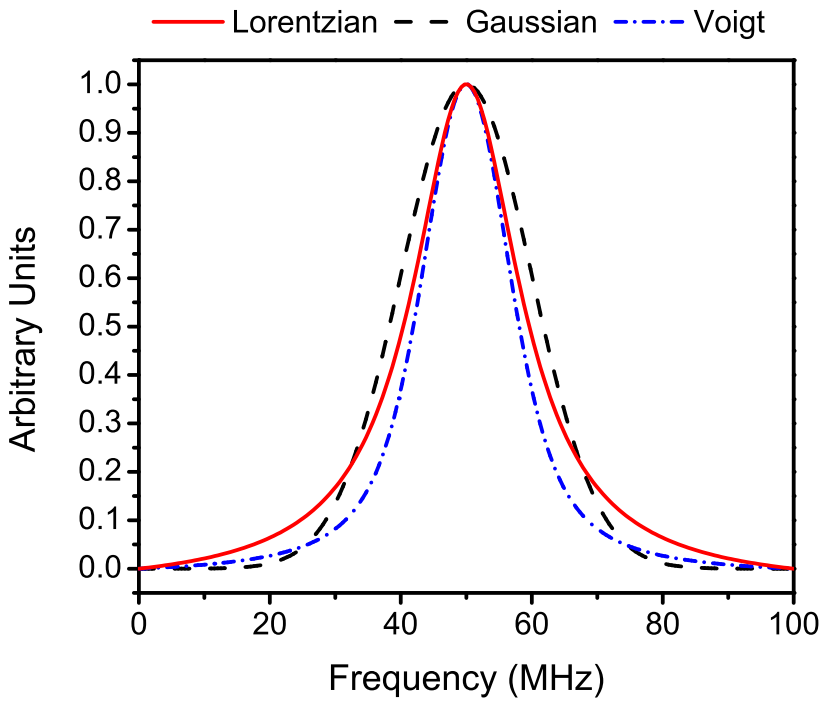

Figure 1.2: Typical Lorentzian, Gaussian and Voigt functions used for line shape analysis, shown as function of frequency.

1.3 Hyperfine Structure

The electromagnetic interaction of electrons with the multipole moments of the nucleus gives rise to atomic hyperfine structure. Fine structure of an atom comes from spin-orbit coupling between the total electron orbital angular momentum (L) and the total electron spin (S) and is described by the total electron angular momentum quantum number, J, where $J = L + S$. The total angular momentum of the electrons must be then coupled with the nuclear spin (I_N) to give the hyperfine energy levels, denoted by the total angular momentum of the atom or ion, F, where $F = J + I_N$ [8].

The fine and hyperfine splitting of ^{43}Ca is shown in Fig. 1.3 as an example. Fine structure energy levels are shown in column (B) and hyperfine structure levels are shown in column (C). The two allowed transitions (absorption) between the fine levels are the D1 ($^2S_{1/2} \rightarrow^2 P_{1/2}$) and the D2 lines ($^2S_{1/2} \rightarrow^2 P_{3/2}$). The allowed transitions between the hyperfine energy levels, according to the rules described in

Sec. 1.2, in D1 are: F=3 → 3, F=3 → 4, F=4 → 3, and F=4 → 4. Whereas, in D2, they are: F=3 → 2, 3, and 4, and F=4 → 3, 4, and 5.

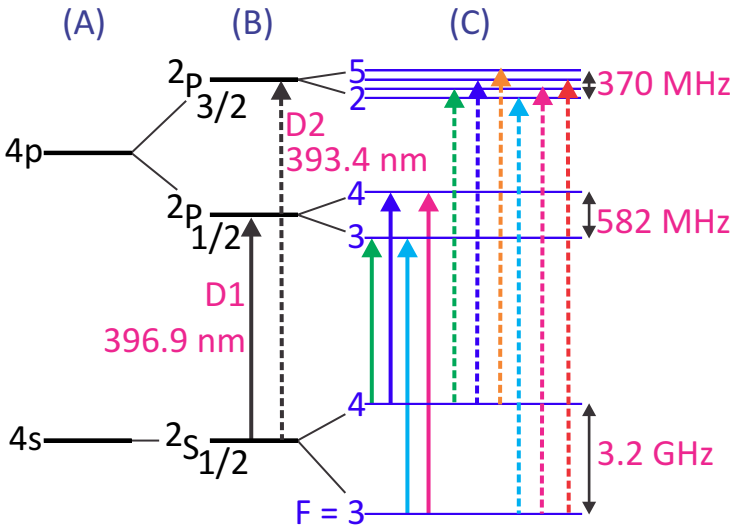

Figure 1.3: Fine and hyperfine structure of ^{43}Ca, nuclear spin $I_N = \frac{7}{2}$. D1 transitions are denoted by solid arrows and D2 are denoted by dashed arrows.

Fine energy level splitting is of order a few THz, while hyperfine splitting is of order hundreds of MHz. A precision method is required to resolve the hyperfine structure levels. Linewidth broadening can cause the hyperfine levels to overlap and not be observeable.

1.4 Collinear Laser Spectroscopy

Collinear laser spectroscopy will be applied at NSCL at the new BECOLA facility, and the photon detection system is the key measurement element for obtaining the resulting hyperfine spectrum. The collinear geometry of the particle beam and the laser beam will allow scanning of the velocity of the ion beam rather than the laser frequencyto bring the system into resonance. The velocity of the beam can be adjusted through application of an acceleration or deceleration voltage in the detection region. The collinear overlap between the laser and the ion or atom beam (for a distance of typically 1 m or greater) provides a long interaction time between the beams.

Velocity Bunching

Ion post acceleration allows increased sensitivity through velocity bunching [9]. The initial kinetic energy spread, ΔE_k, of an ion beam remains unchanged after electrostatic acceleration [9, 10]. As the kinetic energy of the beam ($E_k = \frac{1}{2}mv^2$) increases, the velocity also increases, so that the relative velocity spread (Δv) is smaller at higher ion velocities after acceleration for a given ΔE_k ($\Delta E_k = mv\Delta v$). Velocity bunching allows the Doppler broadening to be reduced to the order of the natural line width, so that the sensitivity and precision of spectroscopy measurements are improved because the fluorescence peaks will have a smaller FWHM.

Doppler Shift

Atoms and ions traveling at a velocity ($v = \beta c$) experience the Doppler-shifted laser frequency at ν' from laser light with a frequency ν_L as;

$$\delta\nu' = \nu_L \frac{\sqrt{1-\beta^2}}{1 \pm \beta}, \tag{1.4}$$

where the "+" sign is applied for a collinear beam geometry and the "-" sign for anti-collinear beams. Here β is the relativistic velocity function given by:

$$\beta = \frac{v}{c} = \sqrt{1 - \frac{m^2c^4}{(eU + mc^2)^2}}, \tag{1.5}$$

where c is the speed of light, m is the particle's rest mass, and U is the accelerating potential.

The laser frequency ν_L applied in collinear laser spectroscopy is typically set to a Doppler-shifted resonance frequency of the particle, ν', so that a transition resonance frequency ν_0 will be absorbed by the atom.

Differential Doppler Shift

The differential doppler shift ($\delta\nu_{diff}$) is the differential change in the frequency in the particle's rest frame per change in the acceleration voltage;

$$\delta\nu_{diff} = \frac{\nu_0}{mc^2(e + \frac{e(mc^2+eU)}{\sqrt{eU(2mc^2+eU)}})}. \tag{1.6}$$

The differential doppler shift gives the relationship between the scanning voltage and the frequency observed by the particle, which allows extraction of physical quantities such as the frequency of a resonance and the splitting between hyperfine energy levels.

1.5 BECOLA Facility

BECOLA is one of the end stations constructed for experiments with thermalized beams at NSCL [3]. At BECOLA, fluorescence from the interaction between laser light and an ion/atom beam will be collected by a photon detection system to measure hyperfine structure of that ion/atom.

A schematic drawing of the BECOLA facility is shown in Fig. 1.4. Laser light is introduced into the beam line through a laser window in the switchyard, shown on the left-side of the figure. A second laser window is located at the end of the beam line. Light transmitted through the second window is stopped in an external beam dump. An ion beam with a kinetic energy up to 60 keV can be introduced into the switchyard using an electrostatic steerer and further transported to the beam interaction region by a spherical electrostatic bend. Collimator systems and Faraday cups can be placed in two beam observation boxes (BOBs) to measure the beam current and to ensure overlap of the laser and ion/atom beams as they pass through the interaction region. The ion beam can also be neutralized in a charge exchange cell (CEC) to generate

an atom beam, if desired [11]. Fluorescence light emitted after the interaction of the laser light with the ion/atom beam is measured by the photon detection system.

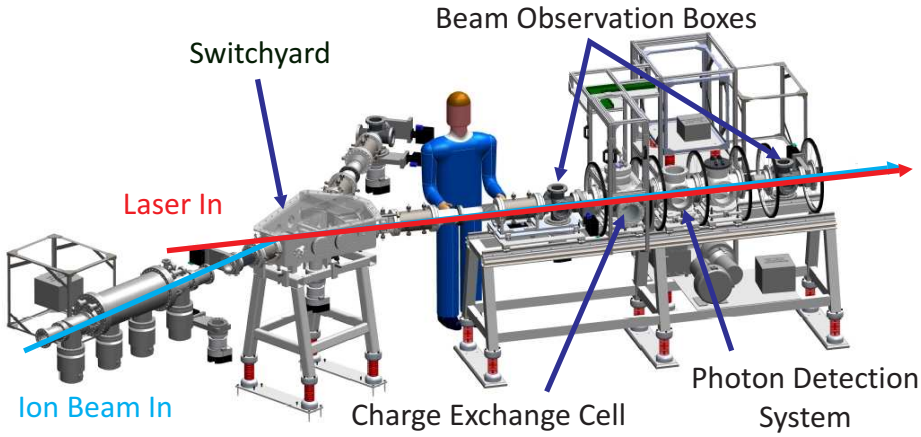

Figure 1.4: The schematic of the BECOLA beam line. The laser beam (red line) and the ion beam (blue line) are collinearly overlapped after the switchyard.

An offline ion source was developed to commission the photon detection system and other components of BECOLA. A stable beam of singly-charged calcium ions was produced by the offline ion source and deflected into the BECOLA beam line. Electrostatic quadrupole lenses were used to control the divergence of the ion beam after the switchyard. The ion beam current entering the interaction region was registered in a Faraday cup that was located in BOB1 and connected to an electrometer. Fluorescence light was collected, as a function of the scanning (i.e. acceleration) voltage, in the photon detection system, that was developed as the main objective of this work. The scanning voltage was applied to all of the components of the photon detection system, since only ion beams were used for the commissioning of the photon detection system reported herein. A Faraday cup in BOB2 located downstream of the photon detection system was used to measure the ion beam that was transmitted through the interaction region. The transmission of laser light through the interaction region was monitored by a power meter located at the beam dump position immediately downstream of the second laser window.

1.5.1 Laser System

The laser system used to excite the fluorescent levels consists of a continuous wave Ti:Sapphire (Ti:Saph) ring laser pumped by a 18 W pump laser operated at 532 nm. The Ti:Saph ring laser has an output power of about 2 W in the wavelength range of 700 - 1000 nm ("red" light). The infrared light from the laser can be used directly for spectroscopy experiments, or it can be transported to a frequency doubler, which produces second harmonic laser light with maximum power of about 200 mW in the wavelength range of 350 - 500 nm ("blue" light) depending on the input wavelength and power from the Ti:Saph. Both the ring laser and frequency doubler were purchased from a commercial vendor, Spectra Physics. The laser light intended for the spectroscopy measurements is passed through a half-wave plate and a polarization cube to set the polarization axis of the light. The polarization cube can also be used to adjust the laser power transported to the experiment. A fiber optic cable is used to transport the prepared laser light over a distance of 26 m to the BECOLA beam line. Fiber optic couplers are used on each end of the fiber optic cable to efficiently transfer the laser light between air and the medium of the fiber optic cable. An image of the output coupler and optics table immediately outside the BECOLA switchyard is shown in Fig. 1.5. The laser light coming out of the fiber coupler is focused by a lens and reflected by two mirrors to a second lens mounted on an adjustable support frame. These two lenses act as a telescoping system and are used to focus and align the laser beam to the ion beam optical axis. A 50:50 laser beam splitting cube is placed after the lens system to split half of the beam to a power meter to monitor the laser power. Two mirrors mounted on fine adjustment mounts are used to align the laser light so that it passes through the center of two pre-aligned irises. The centers of the iris openings are set beforehand to correspond to the beam line optic axis using an optical telescope.

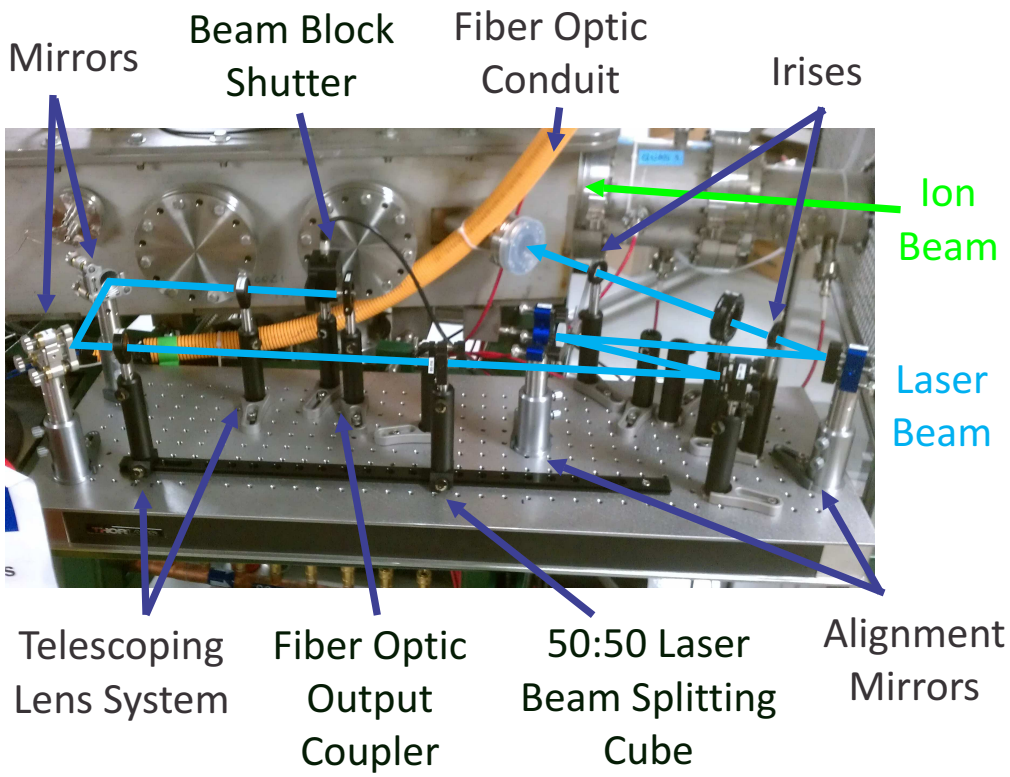

Figure 1.5: Photograph of the laser optics used to tune the laser light into the BECOLA beam line.

1.5.2 Beam Line Diagnostics and Transport

As noted above, two BOBs, which contain detectors for laser and ion/atom beam diagnostics, are located along the BECOLA beam line. One is located upstream (∼1 m) of the photon detection system and the second is downstream (∼1 m) of the photon detection system. The diagnostics in each BOB included a Faraday Cup and beam collimator system. The Faraday cups are used to measure the ion current. The beam collimator system is used to define both the ion beam size and to ensure alignment of the laser beam with the ion beam optical axis. The beam collimators in the BOBs can also be used to define beam size using fixed openings of diameter: 3, 5 and 7 mm. Each collimator is mounted on a linear actuator, which allows the transported beams to be manipulated without breaking the vacuum.

1.5.3 Offline Ion Source

A Colutron plasma offline ion source [12] was used to produce stable calcium beams for the commissioning of the "blue" photon detection system. The ion source was placed upstream of the switchyard. The major components of the source are depicted schematically in Fig. 1.6. Calcium ion beams were produced using calcium metal placed inside a 1.5-inch long, 1/8th inch diameter ceramic tube that served as the charge holder, not shown. The charge holder was recessed in the boron-nitride chamber while the plasma was conditioned. A voltage was applied to the filament to start the plasma. Once the pressure of the source stabilized with the filament running, the charge holder was pushed towards the filament with a push rod, with the goal of evaporating and then ionizing the calcium metal that was placed inside the charge holder. The charge holder was inserted at three different positions relative to the boron-nitride chamber, as depicted in Fig. 1.7. The voltage applied to the filament, typically 7-9 V, was found to be sufficient to evaporate the calcium metal, which was then ionized in the plasma between the filament and anode.

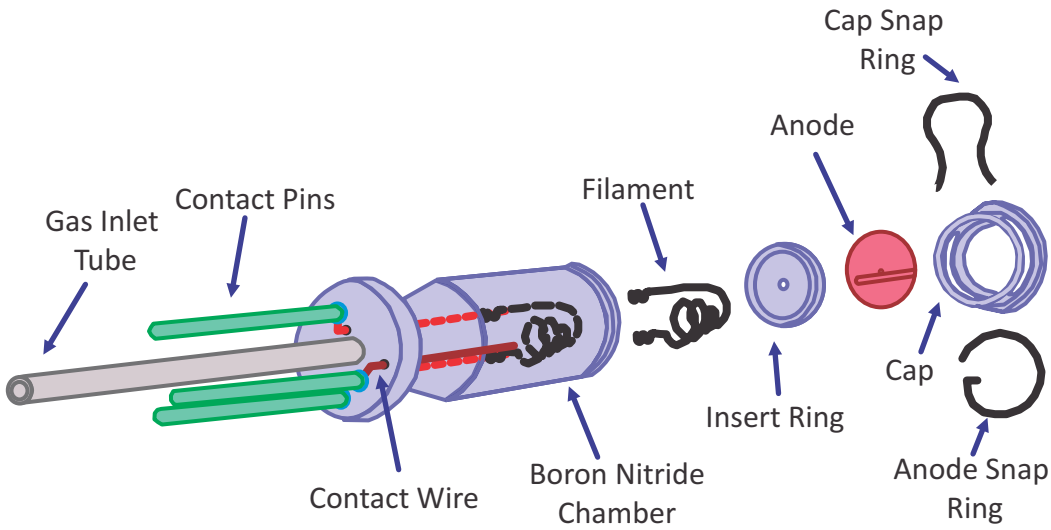

Figure 1.6: Exploded view of the Colutron Plasma Ion Source components. The charge holder is not shown in this view.

The filament used to heat the charge holder and generate the plasma was held inside the boron-nitride chamber by two ceramic spacers. The contact wires were also

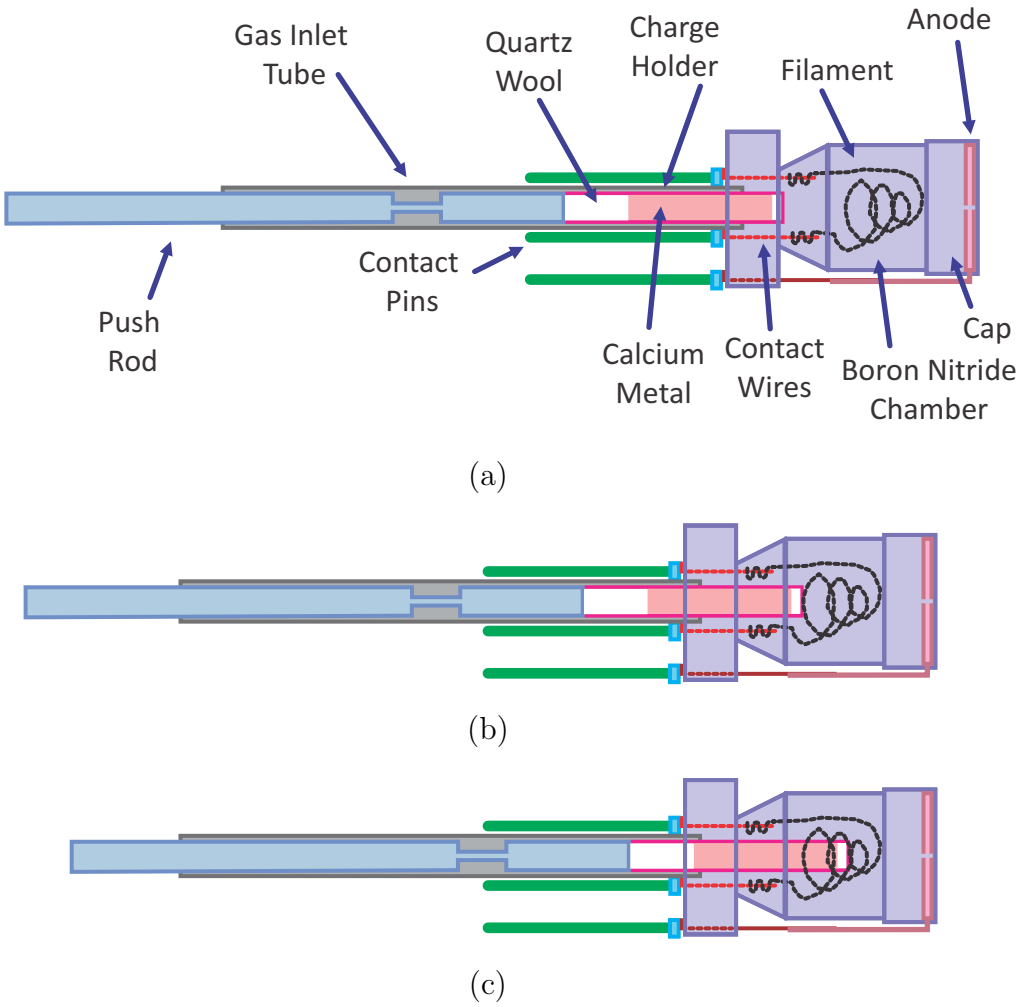

Figure 1.7: Schematic diagram of the modified version of the Colutron ion source used at BECOLA. (a) The ion source with the ceramic charge holder and metal push rod recessed before entry into the chamber. (b) The ion source with the charge holder pushed to the beginning of the filament. (c) The ion source with the charge holder pushed in to the end of the filament.

bent to keep the filament aligned and in place, as depicted in Fig. 1.8.

Calcium ions offered an ideal system for initial commissioning tests of BECOLA and the "blue" photon detection system . The D1 and D2 lines of Ca^+, with wavelengths of 396.9 and 393.4 nm, respectively, are readily accessible with the present laser system. In addition, the calcium atom also has fine structure transitions in the "blue" region of the electromagnetic spectrum, and the same photon detection system could be applied to perform laser spectroscopy on both calcium ions and atoms.

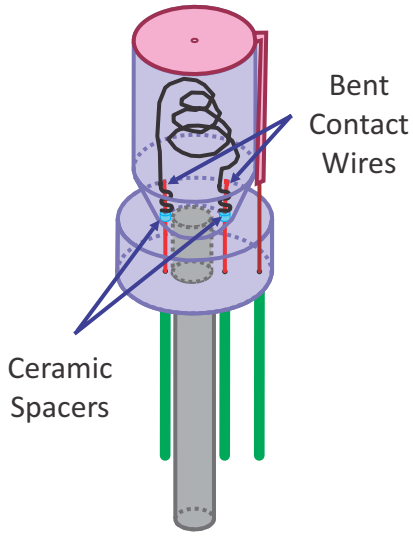

Figure 1.8: The filament of the Colutron ion source. The filament is kept in place by bending the contact wires and using ceramic spacers.

1.5.4 Photon Detection System

The photon detection system that was developed as part of this work was used to collect fluorescence photons emitted from the $^{40}Ca^{+}$ ion beam after interaction with laser light. It consisted of an ellipsoidal reflector that focused the fluorescence light from the first focal point to a photomultiplier tube (PMT) positioned at the second focal point (ellipsoid focusing properties will be further discussed in Sec. 3.2). The PMT then converted the photons to an electrical signal. More details on the photon detection system are provided in the following chapters.

1.5.5 DAQ and Controls

The BECOLA data acquisition system (DAQ) was used to control the scanning voltage applied to the ellipsoidal reflector of the photon detection system, and to read out the electrical signals from the photon detector. The DAQ consisted of a DC amplifier (Matsusada AMP) used to apply a scanning voltage of $\pm$ 10 kV (maximum) to the ellipsoidal reflector. The electrical signal from the PMT was converted to NIM logic signal by a NIM to TTL (Transistor-Transistor Logic) converter and counted by a

scaler. The layout of the DAQ is depicted schematically in Fig. 1.9. The scalar and control of scan parameters were accessed through a graphical user interface (GUI) using the EPICS (Experimental Physics and Industrial Control System) control system [13, 14]. Scan parameters include the scanning voltage range, the step size, the dwell time, and the number of scans to be accumulated. Small step size allows for better data resolution in a scan, while larger step size allows the scanning over a broader voltage range.

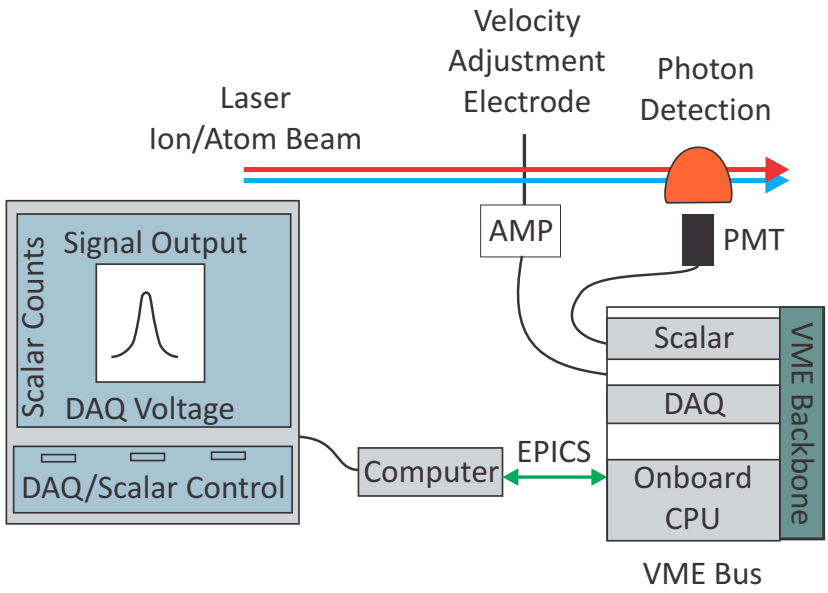

Figure 1.9: The basic layout of the DAQ and controls system for BECOLA.

Chapter 2

Simulation of and Extensions to the Mainz Photon Detection System

2.1 Tools

Optical ray trace simulations of the photon detection system were preformed using the FRED optical engineering software code version 9.10.0 by Photon engineering [15] to optimize the system's performance in BECOLA. The starting point of the simulations was the photon detection system designed by Jörg Krämer at the University of Mainz [16]. The computer-aided design (CAD) file for the Mainz system was imported into FRED and the materials, light sources, and analysis surfaces were defined. The original Mainz configuration file was then modified to find an optimal geometry for the ellipsoid, light collection, and photomultiplier tube (PMT). The figure of merit used was the signal to noise ratio (S/N), where signal (S) was the number of fluorescence photons simulated to enter the PMT and noise (N) was defined as the square root of the simulated stray light photon count at the face of the PMT.

2.1.1 Geometry Used in FRED

The photon detection system imported from the Mainz CAD file was centered inside a 6-way cross vacuum chamber, and two additional vacuum chambers were included in the model as sources of stray laser light reflecting along the beam line.

The signal light sources were generated from a 3-mm diameter cylinder placed along the beam direction that included the first focal point of the ellipsoidal reflector. Two cylinders were created in order to model the fluorescence light from ions or from atoms. The first cylinder started at the upstream inner HV drift tube and ended at the downstream inner HV drift tube describing the region where the scanning HV would be applied for an ion beam. The second cylinder started halfway through the charge exchange cell vacuum chamber to include the region where fluorescence would start for an atom beam. The atomic fluorescence source light cylinder passed through the photon detection system chamber and ended at the end of the third chamber (see Fig. 1.4 for the locations in the conceptual design of BECOLA). The photon detection system geometry, as developed in FRED, is presented in Fig. 2.1.

Stray light was assumed to have two contributions in the simulations performed here: laser light reflected along the beam line and laser light scattered by the first beam line aperture. The first contribution was modeled by light sources on the inner surfaces of the three vacuum chambers. The second stray light source was modeled with a ring-like source on the inner edge of the first beam line aperture.

Random rays were programmed to be emitted isotropically from the surface of the light source cylinder to simulate the fluorescence given off by the particle beam, and from the inner surfaces of the vacuum chambers to model reflection of stray laser light. A total of 1,000,000 rays were traced for the signal light source, at wavelength values of 397 nm and 800 nm. Photons were lost as they interacted and were absorbed by surfaces in the simulation, and they were also reflected and transmitted through materials based on their reflective properties.

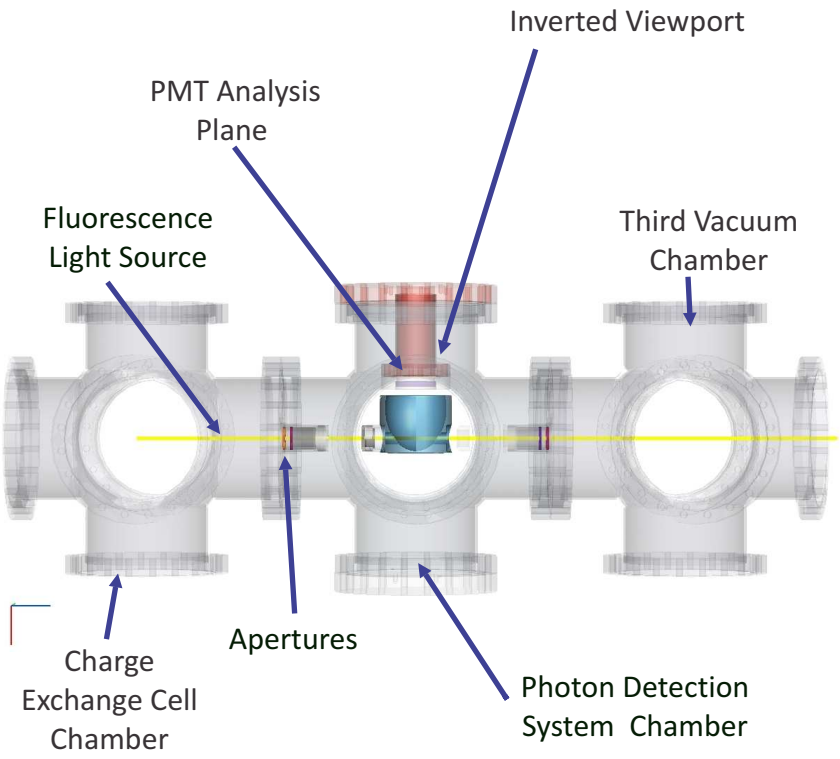

Figure 2.1: Engineering drawing of the geometry imported into FRED for ray trace simulations of the detection system.

Analysis planes were defined at the second focal point of the ellipsoidal reflector for reference and at the entrance to the PMT to count the deposited photons.

2.1.2 Inputs and Constraints

Surfaces in the FRED geometry can be defined in a variety of ways. Lens materials were already programmed into FRED, as were common optical polymers, air, and vacuum. Quartz, glass and acrylic were defined using the preset material designations. Other materials were defined using the real and imaginary refractive indexes for the wavelength of interest. Fresnel's equation for reflection of a plane wave normal to a plane surface between vacuum and a material with complex index of refraction is used within the FRED code to calculate the reflectivity, R, from the refractive indices of a material, with the expression:

$$R = \frac{(n-1)^2 + k^2}{(n+1)^2 + k^2}, \tag{2.1}$$

where n is the real component of the refractive index and k is the complex component of the refractive index for the material.

After a material was defined, coating and ray trace properties were assigned. Surface coating can be used to define the surface as transmissive, reflective or absorbing. Options for ray tracing included transmitting rays or stopping all rays once they hit the surface. The "stop all rays" option was helpful for analysis, because it allowed the photon distributions striking a surface to be examined. Rays could also be set to change visualization colors once they interacted with a surface, so rays that interacted in different ways with the material could be identified. This visualization option was used to ensure that surface materials were correctly assigned in the FRED code.

Analysis surfaces were defined to examine the ray distributions on a plane and were set to record all rays that were stopped by a surface. Light sources with wavelengths of 397 nm and 800 nm were used for both the signal (fluorescence) and stray light simulations. The power from each light source was arbitrarily set to 1 W. Only one wavelength was traced and analyzed at a time.

The irradiance distribution on the surface of a chosen analysis plane was selected

for the present analysis and was used to deduce the number of photons and the S/N. A distribution of the irradiance (power over area) for the rays stopped on the surface was provided by the FRED code after each run as visual output. The number of photons was proportional to the power:

$$P = \sum_f n_f E_f. \tag{2.2}$$

Here P is the power, n_f is the number of photons with frequency f, and E_f is the energy of a photon of frequency f. The simulation results for a given wavelength were compared directly with all other wavelength simulation results, since all simulations for a given frequency started with the same number of photons.

2.2 Typical Output

The photon distributions at the second focal plane indicated a distinct physical separation of the signal and stray light distributions. The irradiance distributions of the signal and stray light at the second focal plane for a 76.2-mm ellipsoidal reflector, which was eventually used in the photon detection system for BECOLA, are shown for example in Fig. 2.2. An iris system at the second focal plane could be used to take advantage of the physical separation between the distributions and increase the S/N by blocking the stray light that is concentrated at the outer edge of the focal plane.

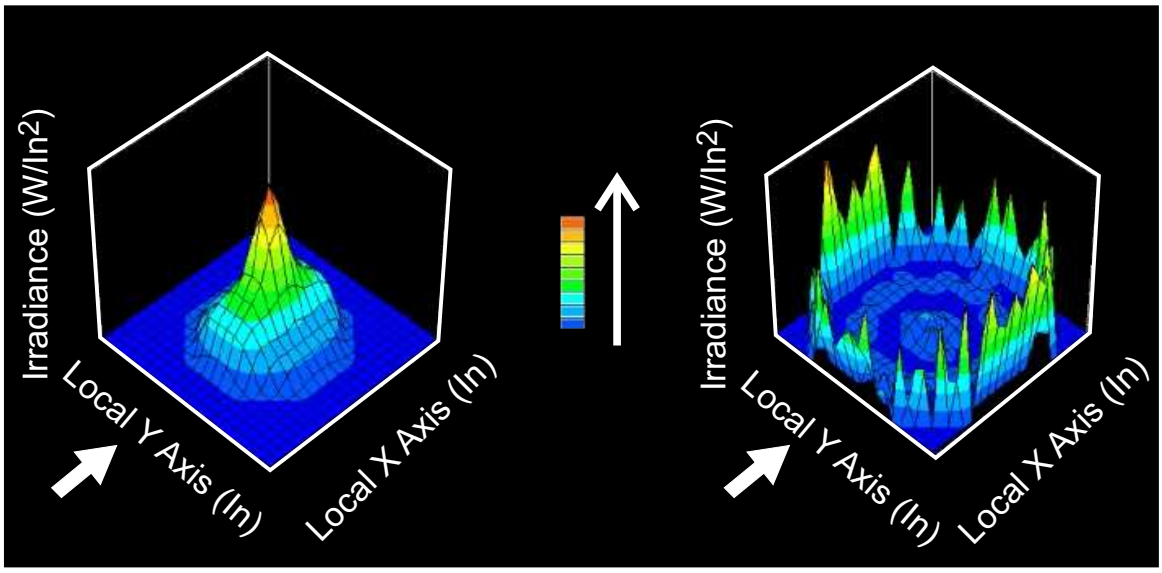

Figure 2.2: Simulated signal (left) and stray light (right) distributions at the second focal plane of 397 nm light for the photon detection system that includes a 76.2-mm ellipsoidal reflector.

2.3 Optimizing System Geometry

2.3.1 Reflector Size

The Mainz system consisted of an ellipsoidal reflector with a 50.8 mm photon collection region (minor ellipsoid axis). The photon collection length was taken to be the distance that the laser and particle beam interacted to give off fluorescence inside the reflector. The reflector's photon collection length was varied in the simulations with FRED to optimize the light collection and S/N of the detection system. A 127-mm long collection length was selected for use in the simulation because it was the largest possible reflector that could fit into the planned BECOLA beam line. A 76.2 mm collection length system was also created and simulated to get a performance measure for a reflector in-between the two other sized systems.

The goal of the simulations for the different reflector lengths was to find the optimal light collection geometry, again using S/N as the figure of merit. Signal and stray light distributions at the second focal plane analysis surface were analyzed at 397 nm and 1 Watt of power from the signal source for 50.8 mm, 76.2 mm and 127 mm

diameter reflectors. Stray light was also analyzed at 397 nm with an initial power of 1 Watt from each inner surface of the three vacuum chambers in the simulation. The three different reflector geometries were tested with both 100% and 0% reflective inner surfaces of the vacuum chambers to cover both the worst and best case scenarios for the stray light production. The best case was assumed to be achievable, in practice, by black plating the inside of the vacuum chambers.

The results of relative S/N for signal and stray light distribution irradiances at the second focal point for the three simulated reflector geometries are shown in Fig. 2.3. The S/N appears to saturate for the 76.2-mm reflector, and S/N can also be increased when a 25.4 mm diameter iris is placed at the second focal plane. Saturation of the signal is expected for larger collection lengths, since the signal distribution is well focused at the second focal point, and the shoulders along the beam axis (due to the pencil like distribution along the beam path) contribute only a small fraction of the total light collected at the second reflector focal plane. The gain from the shoulders at larger sizes appears to stop being significant at a collection length of 76.2 mm. The stray light distribution is expected to decrease for larger collection dimensions because as the surface area inside the reflector was increased, the beam path opening size remains constant. The 76.2 mm reflector was employed in all subsequent simulations described herein, since this collection length was found to have the optimal S/N.

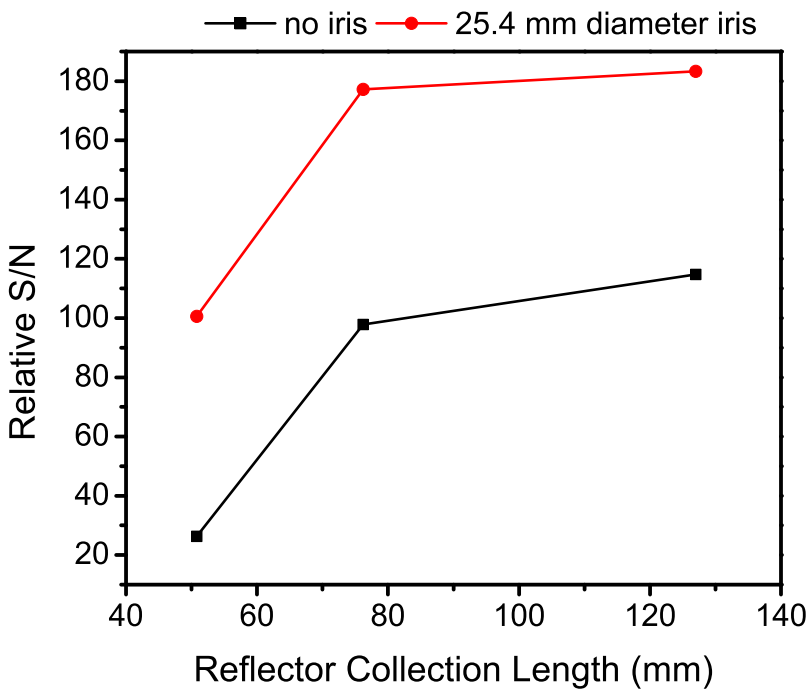

Figure 2.3: Relative S/N values obtained by simulation for 397 nm light collected at the second focal plane for the three collection lengths specified in the text. The upper points include the effect of an iris at the second focal plane.

2.3.2 Irises at the Second Focal Plane

An iris system of variable size was also included in the simulated geometry. The iris was positioned at the second reflector focal plane and the iris opening size was varied to optimize the S/N for light collection. The simulation results are shown in Fig. 2.4. The S/N was found to increase as the open iris area was increased for irises having a circular geometry. Iris systems with a rectangular geometry were also simulated and the S/N doubled as the area was doubled from a 12.7 x 6.35 mm rectangular iris to a 25.4 x 6.35 mm rectangular iris.

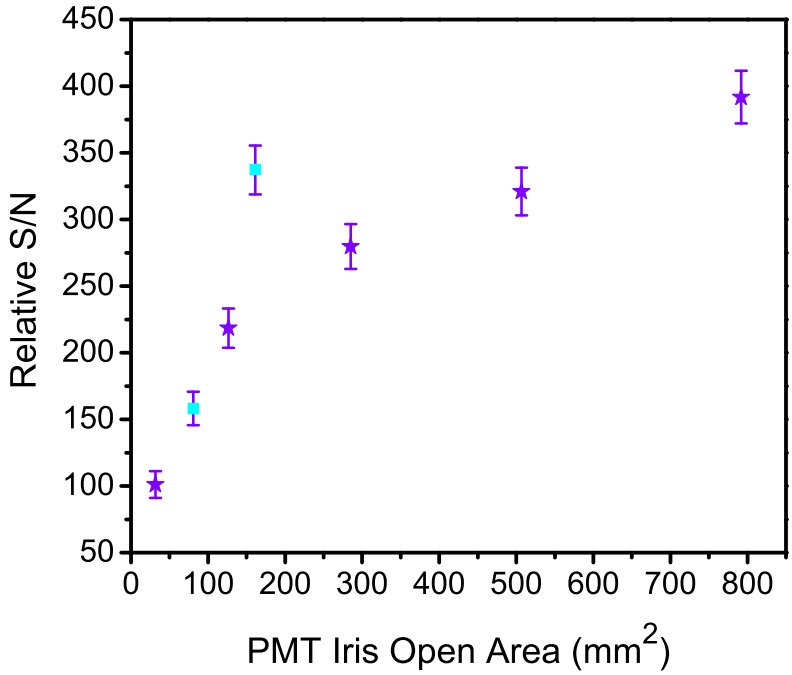

Figure 2.4: S/N ratio, as a function of iris open are at the PMT face, deduced from simulated signal and stray distribution irradiance at the second focal plane of 397 nm light for the 76.2-mm reflector. The stars denote circular irises while the rectangular points denote rectangular irises.

2.3.3 Beam line Apertures

The possible placement of beam line apertures was studied in the simulations to determine the potential impact on S/N. Apertures were placed both upstream and downstream of the ellipsoidal reflector, inside the inner drift tubes (see Fig. 2.5). The most upstream aperture was designed to cut the laser halo, but scatters the laser light. The subsequent apertures were designed to block light scattered by the first aperture and to reduce the opening angle into the reflector through which stray light can enter.

Laser light was assumed to only be scattered by the first aperture. Backscattering was not considered in the simulations. Aperture configuration (a) in Fig. 2.5 was not simulated because there was no aperture to include a stray light source. Aperture configuration (c) was shown to have the highest S/N of the configurations simulated.

This is reasonable, since a majority of the simulated stray light comes from the first beam line aperture and the additional upstream apertures serve to block more of the scattered (stray) light.

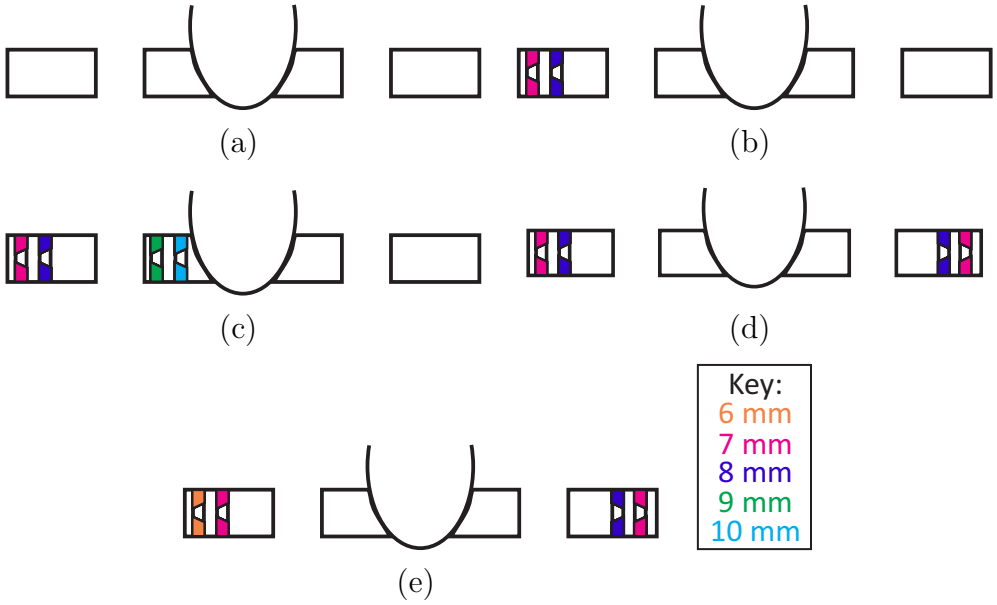

Figure 2.5: Conceptual layout of the inner drift tube aperture configurations that were simulated in the present work. The laser light passes from left to right through the center of the apertures and through the first focal point of the reflector.The sizes of the apertures are indicated by their color.

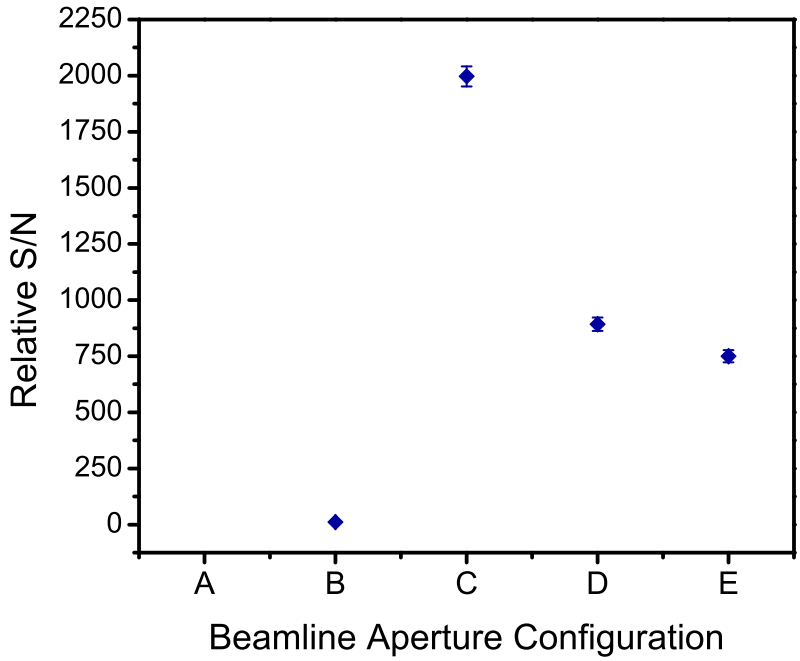

Figure 2.6: The S/N ratio as a function of aperture configuration deduced from simulated signal and stray distribution irradiance at the second focal plane for 397 nm light with the 76.2-mm reflector.

2.4 Summary of Results

The FRED optical engineering software was used to simulate the performance of the "blue" photon detection system for BECOLA. An evaluation of the S/N as a function of the length of the ellipsoidal reflector showed that optimal performance could be achieved with a 76.2-mm interaction length. Therefore, a 76.2 mm reflector has been implemented for the BECOLA facility based on the simulation results. The simulation results also revealed a distinct physical separation of signal and stray light at the second focal plane of the ellipsoidal reflector. These results suggest that an iris system can be used at the second focal plane to optimize the S/N. Such an iris system was simulated with the FRED code and confirmed the improved light collection performance with restricted opening at the second focal plane. An adjustable iris system was constructed and placed in front of the PMT at the second focal plane of the BECOLA photon detection system as a result of these simulations. Simulation

results of beam line aperture configurations indicated, not surprisingly, that beam line aperture locations have a significant effect on S/N. The configurations labeled (a)-(e) were tested experimentally to verify the simulations, and the results of the tests are presented in Chapter 5.

Chapter 3

Design of the BECOLA Photon Detection System

3.1 Design

The design of the photon detection system was based on the results of the simulations described in the previous chapter, starting from the tested design of the Mainz system and including new constraints at BECOLA. An added feature is that the BECOLA laser system consists of a Ti:Sapphire laser and frequency doubler, which can produce light in the wavelength ranges of 700-1000 nm and 350-500 nm, respectively, and the two laser wavelength ranges require different PMTs for efficient photon detection. However, the light collection system for the interaction region was designed to be useful for both wavelength ranges. The photon detection system can work for ion beams by scanning a high voltage (<10 kV) applied to the interaction region and for atom beams by applying the high voltage to the CEC. An electrically-conductive material was selected for the reflector to permit application of high voltage for scanning purposes, and it was designed to be isolated from ground.

3.2 Interaction Region and Light Collection

The interaction region of the BECOLA facility is the region between the two BOBs where the ion/atom and laser beams are collinearly overlapped for about 3 meters. Emission of fluorescence light for atomic beams begins after neutralization, and for ion beams the fluorescent region begins upon collinearity between the ion and laser beams. For both atom or ion beams, the light collection region is defined by the 76.2-mm length of the reflector.

The geometrical properties of an ellipsoid ensure that all photons emitted at the first focal point are reflected to a second focal point [17], as depicted in Fig. 3.1. The collinearly overlapped ion/atom and laser beams pass from left to right through the first focal point of the ellipsoid. Fluorescence photons (denoted by dashed lines) are emitted along the beam path, so not all photons are emitted at the first focal point. The ellipsoidal reflector is efficient at focusing any fluorescence emitted inside the collection region to the second focal plane [16, 17]; however, stray light will be focussed as well [18].

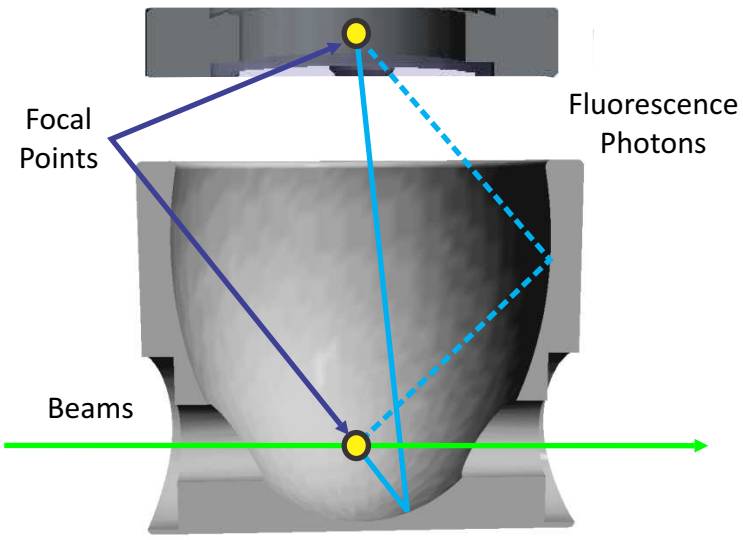

Figure 3.1: Representation of the geometrical properties of an ellipsoidal reflector. Fluorescence photons emitted at the first focal point are reflected to the second focal point. The reflector has rotational symmetry around the vertical axis.

3.2.1 Ellipsoidal Reflector Specifications

The geometrical properties of the reflector constructed for the BECOLA photon detection system are shown in Fig. 3.2. The minor axis of the ellipsoid has a radius of 38.10 mm, a major axis radius of 53.34 mm, and the focal length is 74.68 mm. The focal length was chosen to allow for an insulation gap of 18.03 mm between the top of the reflector and the inverted viewport window flange. The reflector has rotational symmetry along the vertical axis to increase solid angle coverage.

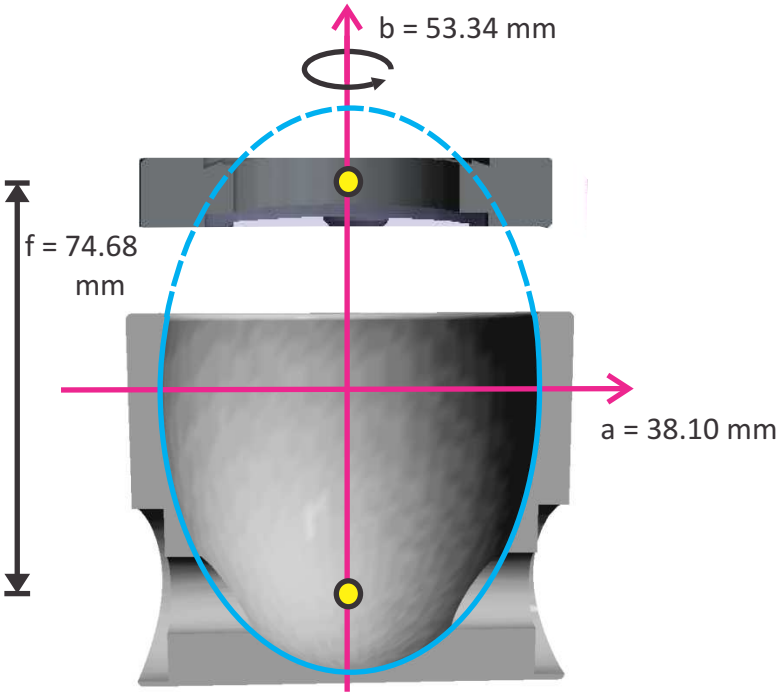

Figure 3.2: The geometrical properties of the BECOLA ellipsoidal reflector. The reflector has rotational symmetry around the vertical axis.

3.2.2 Ellipsoidal Reflector Material

The ellipsoidal reflector must be reflective in both the "blue" and "red" system wavelength regions. The reflectivity curves in the required wavelength range for the metals that were considered are shown in Fig. 3.3. The reflectivities for all three metals are

high in the "red" region but the reflectivities of silver and copper drop off rapidly as they approach the "blue" wavelength range, thus aluminum was chosen for the ellipsoidal reflector material.

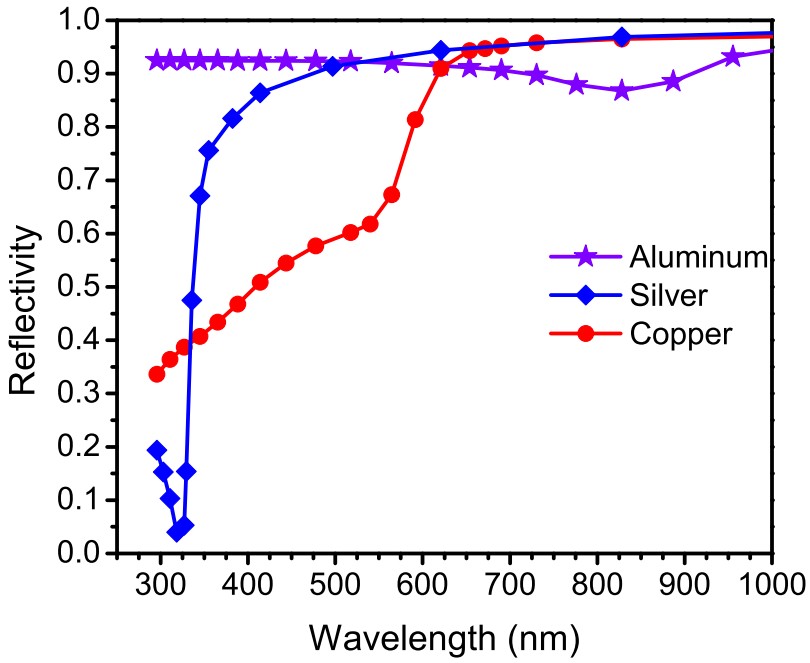

Figure 3.3: Reflectivity curves of the metals considered for the ellipsoidal reflector in the wavelength regions available at BECOLA. Silver is depicted by diamonds, copper by circles and aluminum by stars.

Aluminum is a soft metal and is difficult to polish to a mirror-like surface. Machine polishing was attempted, but deep scratches were found on the inner reflector surface. In the end, the reflector was hand polished using micro-mesh polishing pads [19] and was finished using a Mother's Power Ball Mini [20] with Simichrome metal polish [21]. The reflectivity was tested using the BECOLA laser system and values of ∼68-72% were achieved at 794 nm (representative "red" wavelength) and ∼58-62% at 397 nm (representative "blue" wavelength). A photograph of the finished reflector is shown in Fig. 3.4.

Aluminum oxidizes in air over time; however, the reflector is generally kept under vacuum, which will help slow the oxidative process. Touch-up polishing may be

required to remove the layer of aluminum oxide that forms, and also to remove any alkali metal that leaks into the reflector from the CEC.

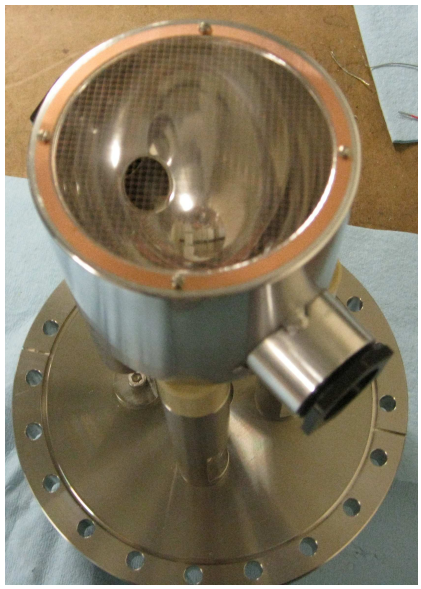

Figure 3.4: Photograph of the ellipsoidal reflector after hand polishing.

3.3 Stray Light Reduction

The sensitivity of the photon detector to stray light was noted by the Mainz group to be a critical hurdle for experimental work [16, 18]. Increased stray light leads to a reduced S/N, which is problematic for low counting rates expected for rare isotope beams. Several features were implemented at the BECOLA beam line to reduce stray light levels. (1) The inside of the detection system vacuum chamber was black plated. (2) An outer drift tube was added around the inner drift tubes. The outer and inner drift tubes were also black plated to minimize scattering of stray light inside the chamber that houses the BECOLA photon detection system. (3) Apertures were placed inside the inner drift tubes to cut the laser halo and to block out the resulting scattered laser light as discussed in Sec. 2.3.3. The apertures were similarly painted black to decrease their reflectivity and reduce stray light. Additional details on the beam line apertures are given in Sec. 3.3.1.(4) Following the simulation results, the

second focal plane was designed to accept an iris of variable opening geometry and size. The iris is placed immediately in front of the "blue" PMT as described in Sec. 3.3.2.

3.3.1 Beam line Apertures

Apertures placed inside the inner drift tubes were used to cut the laser halo and to block the resulting scattered laser light. The apertures also reduced the stray light that entered the open ends of the ellipsoidal reflector. The beam line apertures were fabricated out of aluminum and anodized black. Anodized aluminum is not electrically conductive, and can charge up when hit by an ion beam. The anodized apertures were coated with graphite paint to make them conductive to avoid any beam charging and possible beam deflection.

The beam line apertures were designed to be placed in pairs inside the inner drift tubes, as depicted in Fig. 3.5. The apertures all have an outer diameter of 27.7 mm and are 3.0 mm thick with a conical opening. The inner diameters of the smaller opening that were fabricated are 7 mm, 8 mm, 9 mm, and 10 mm, where the angle is 45° between the smaller and larger diameter opening. Two 7 mm inner diameter apertures are shown in Fig. 3.6 after application of graphite paint.

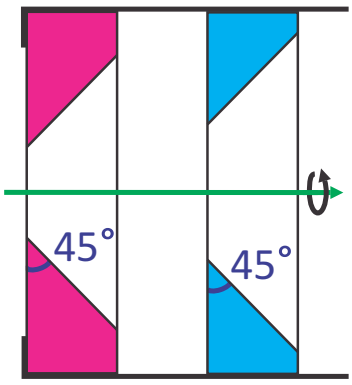

Figure 3.5: Schematic view of the placement of a pair of beam line apertures.

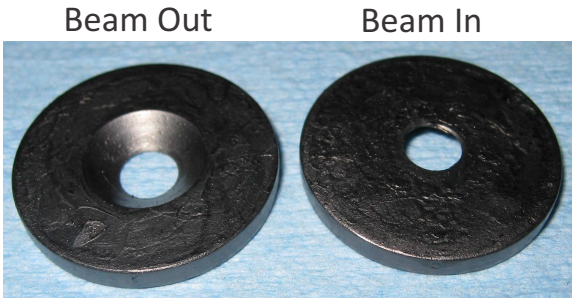

Figure 3.6: Photograph of two 7 mm inner diameter beam line apertures after being painted with graphite paint to be conductive.

3.3.2 Irises for the PMT

An iris can be placed at the second focal plane of the ellipsoidal reflector, as discussed in Sec. 2.3.2. The irises were fabricated from 0.79 mm thick aluminum disks with a 44.1 mm outer diameter. The inner opening size and geometry were varied. Irises with inner opening diameters of 31.75 mm, 25.4 mm, 19.05 mm, and 12.7 mm were fabricated. After the machining process, the irises were black anodized to absorb stray light. Several irises were not machined (6.35 mm in diameter, 6.35 $\times$ 12.7 mm, 6.35 $\times$ 25.4 mm) but rather were hand-made from black aluminum foil. A teflon holder that mounts on the PMT was designed to hold the iris in place at the second focal plane and allowed for efficient switching of irises during experiment. Shown in Fig. 3.7 are the 12.7 mm diameter and the 6.35 $\times$ 25.4 mm rectangular irises, as they were placed inside the teflon holder. The irises fabricated from the black foil were attached to the teflon holder using double-sided tape.

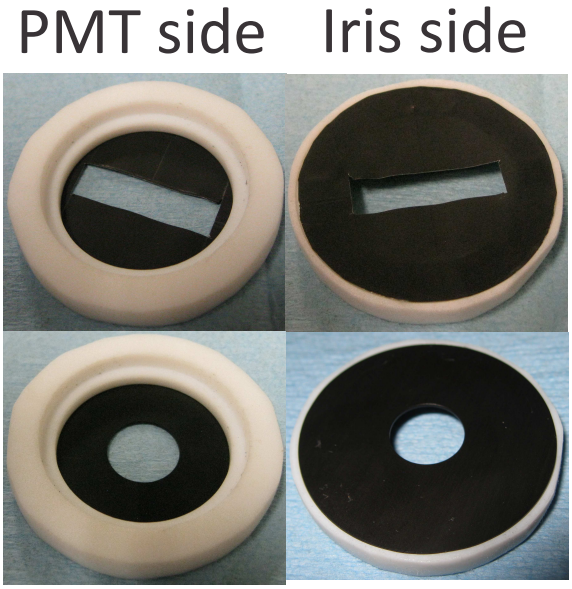

Figure 3.7: Photographs of the 12.7 mm (machined) in diameter circular iris and the 6.35 × 25.4 mm (hand-made) rectangular iris inside the teflon iris mounting system. The PMT side of the teflon holder is shown on the left and the side adjacent to the inverted viewport window, where the iris is mounted, is shown on the right.

3.4 PMT Selection

The PMT selection was based on a review of the active area, quantum efficiency (QE), dark count levels, and usable wavelength range as listed by the manufacturers. Dark count levels are due to leakage current between the dynodes and to thermal electrons produced by the photocathode. thermal electron production depends on ambient temperature, photocathode material, and active area. The usable wavelength range depends on the photocathode material. The QE is the probability that a conversion electron will be produced at the photocathode for each photon that hits the active area and is another property of the photocathode material. The usable wavelength regions for different photocathodes served as the "first criterion" for PMT selection, followed by the active area as well as dark count levels.

The "blue" wavelength region had multiple options for photocathode materials, and many PMTs are available in photon counting module forms. A photon counting module has high sensitivity to detect individual photons, and includes built-in elec-

tronics to amplify the signal and apply a voltage threshold to minimize the dark count levels. Simulated signal light distributions at the second focal plane of the ellipsoidal reflector (see Fig. 2.2) showed a peak in the distribution that covered an area of ∼24 mm in diameter around the focal point, with a spread along the beam axis. An active photon counting area greater than this dimension may lead to an increase in the dark count rate. Therefore, a PMT with a 25.4-mm diameter active area was thought to best match the main area of fluorescence collection at the second focal plane, while discriminating against dark counts. A Hamamatsu H11123 PMT was chosen to detect photons in the region of 300-500 nm ("blue"). It is a head-on PMT with a 28 mm diameter, and a quantum efficiency of 17.6% at ∼400 nm. At room temperature, the expected dark count rate is 70 per second.

By comparison, there were fewer photocathode material options for the "red" wavelength region (700-1000 nm). The "red" photocathode materials also tend to have higher dark count rates, since they produce more thermal electrons at room temperature. Therefore, it was imperative to select a PMT with a reduced active area. Additional simulations were performed with the FRED code to compare available PMTs for "red" light optimizing QE and active areas. As a result of the simulations, the PMT selected for detection of red light was the Hamamatsu R10699. The R10699 is a side-on PMT with an active area of 8 x 24 mm. The PMT is designed to have good efficiency over a broad wavelength range (185 nm to 900 nm). The quantum efficiency at 800 nm is reported to be 9%. The measured dark counting rate at room temperature is below 10,000 counts per second, but depends on the voltage threshold.

The "red" PMT would also be applicable for detection of "blue" light where the QE increases to ∼ 30% at 400 nm. However, the R10699 has a smaller active area and higher dark count levels at room temperature than the H11123 PMT chosen for "blue" light collection; therefore, the R10699 would not be as sensitive to individual photons in the "blue" region.

3.5 "Blue" Light Detection System

The mechanical design of the light detection system for fluorescence photons in the "blue" region of the electromagnetic spectrum is illustrated in Fig. 3.8.

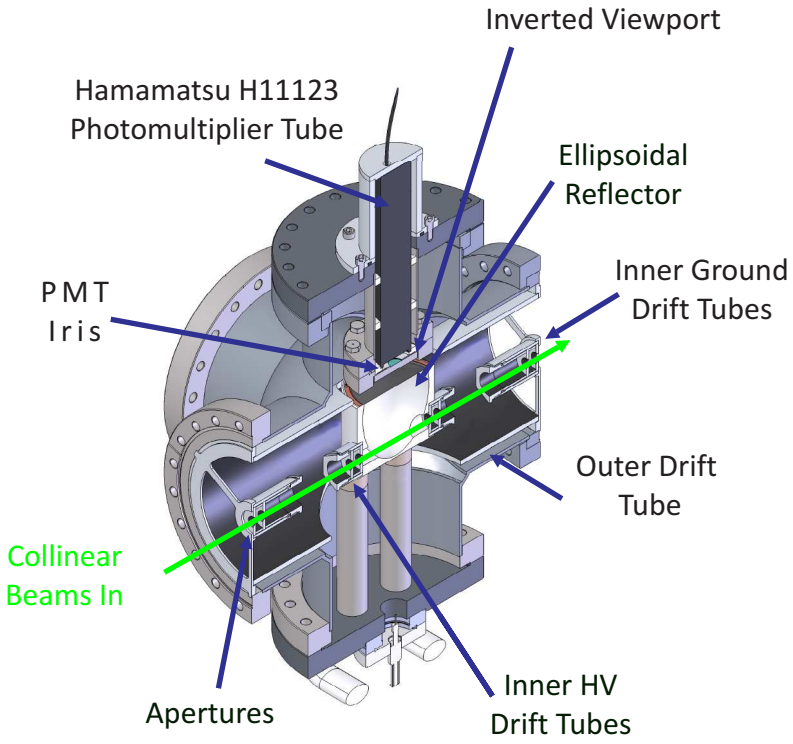

Figure 3.8: The Mechanical design drawing of the blue photon detection system for BECOLA.

The light collection region is 76.2 mm long. As indicated above, the reflector was fabricated from aluminum and hand polished to a mirror-like surface. The collinearly-overlapped laser and atom/ion beams enter the detection system through the inner ground drift tube, which holds the beam line apertures to cut the laser halo and resulting scattered laser light. The inner ground drift tube is welded to the outer drift tube as depicted in Fig. 3.9. The beams then pass through the inner high voltage drift tube, which was welded to the reflector. The reflector itself is mounted on insulated legs, which are attached to a flange to allow removal and servicing of the reflector and the beam line apertures. A high voltage feedthrough on the flange is used to connect a variable scanning voltage to the reflector. A thin copper mesh (with 95% trans-

mission for light) is placed on top of the reflector to ensure a uniform voltage inside the reflector. Fluorescence emitted along the collection region inside the reflector is reflected through a quartz inverted viewport window and to the second focal plane.

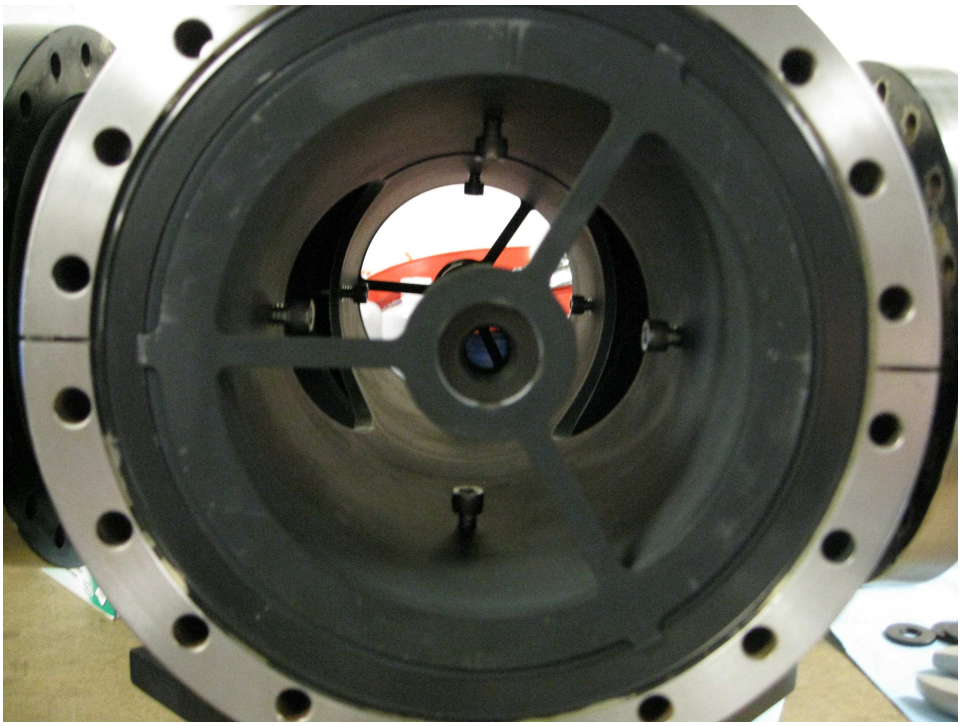

Figure 3.9: Photograph of the vacuum chamber with only the inner and outer drift tubes in place. The beam direction is into the paper through the aperture inside the inner ground drift tube.

As detailed in the previous section, a Hamamatsu H11123 PMT is used to detect photons in the region of 300-500 nm at the second focal plane of the ellipsoidal reflector. The PMT is centered inside the inverted viewport tube by two teflon rings, and ambient light leaks from the experimental area are blocked by a PMT enclosure. The "blue" PMT, enclosure, and teflon rings are depicted in Fig. 3.10.

An iris can be placed in front of the "blue" PMT as a means to reduce stray light from reaching the PMT. Details of the iris system were provided in Sec. 2.3.2 and 3.3.2.

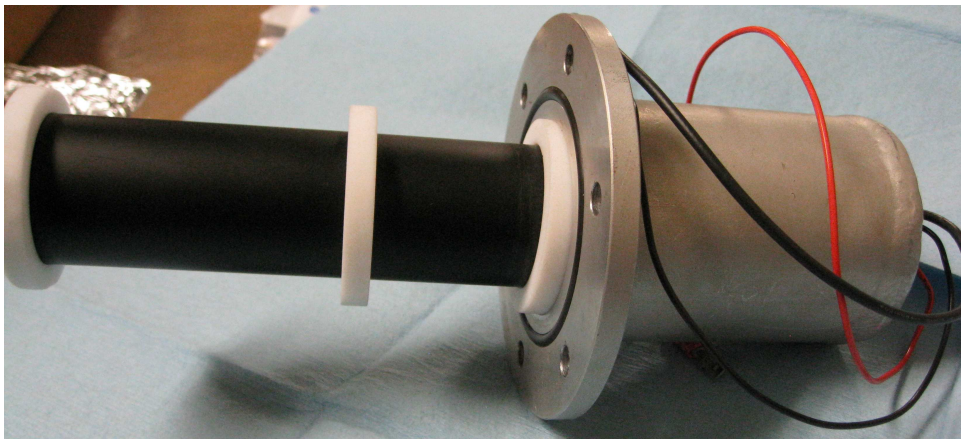

Figure 3.10: Photograph of the "blue" photon detection system PMT, PMT enclosure, and teflon rings used to center the PMT inside the inverted viewport.

3.6 Red Light Detection System

The design of the photon detection system for the "red" region of the electromagnetic spectrum is depicted in Fig. 3.11. The "red" system has essentially the same geometry as the "blue" system. The iris system for the "red" system is placed in the same location as the "blue" system; just above the inverted viewport at the second focal plane of the ellipsoidal reflector.

The side-on arrangement of the R10699 PMT is not compatible with the housing designed for the H11123 head-on PMT or with the inverted viewport tube geometry. Therefore, the "red" light PMT was placed on top of the viewport tube. A tubular silver mirror was used to guide photons from the second focal point to the entrance window of the PMT. The PMT was surrounded by a water-cooled, stainless steel enclosure to keep it at constant operating temperature, as depicted in Fig. 3.12. The PMT base is outside of the stainless steel cooling enclosure, since the base generates significant heat and would negatively impact stable operation of the PMT.

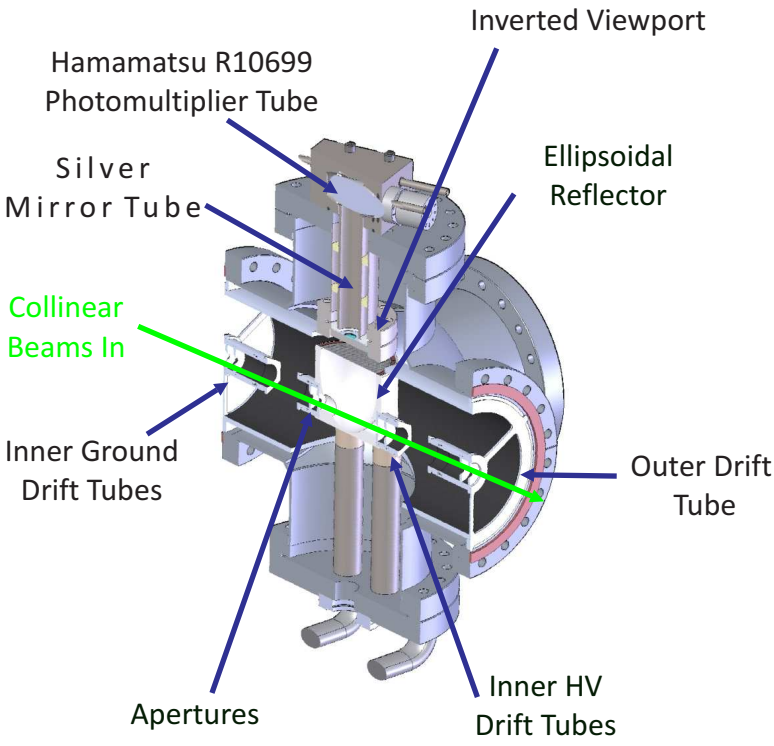

Figure 3.11: The Mechanical design drawing of the red photon detection system for BECOLA.

Figure 3.12: A photograph of the "red" photon detection system PMT enclosure attached to the photon detection system vacuum chamber.

Chapter 4

Calcium Ion Beam Spectroscopy and Commissioning of the "Blue" Photon Detection System

4.1 Commissioning Introduction

The "blue" photon detection was commissioned by collecting fluorescence light from Ca^+ ions in the BECOLA system. Specifically, the fine structure of the 4s $\rightarrow$ 4p atomic states in $^{40}Ca^+$ was observed. The wavelength of the electronic transition is 397 nm. The fine spectrum was collected by counting fluorescence photons with the "blue" PMT as a function of the scanning voltage applied to the ellipsoidal reflector.

4.1.1 Calcium Ion Spectroscopy

The stable isotopes of calcium are: ^{40}Ca (96.941%), ^{42}Ca (0.647%), ^{43}Ca (0.135 %), ^{44}Ca (2.086%), ^{46}Ca (0.004%), and ^{48}Ca (0.187%). The even-even calcium isotopes have a ground state nuclear spin of 0 and therefore exhibit no hyperfine splitting. The fine structure of ^{40}Ca is shown in Fig. 4.1 as an example. The allowed electric dipole

transitions between the fine structure levels are the D1 line ($4\ ^2S_{1/2}$ to $4\ ^2P_{1/2}$) and the D2 line ($4\ ^2S_{1/2}$ to $4\ ^2P_{3/2}$).

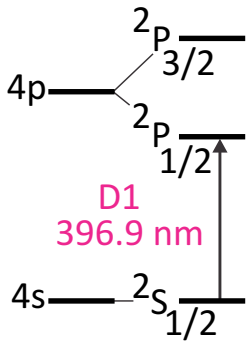

Figure 4.1: Schematic representation of the fine (and hyperfine) structure of ^{40}Ca, which has a ground state nuclear spin $I_N = 0$.

The lifetime of the D1 line of $^{40}Ca^+$ is known to be $\tau = 6.978 \pm 0.056$ ns, which corresponds to a natural line width of $\delta\nu_{nat} = 22.8081$ MHz. For the D1 line in $^{40}Ca^+$ at a beam energy of 15 keV, the differential Doppler shift is 22.62 MHz/V.

4.1.2 Commissioning Set-up

BECOLA Beam line

Stable calcium ions were produced using a commercially available Colutron plasma ion source described in Sec. 1.5.3. Calcium metal was placed in a ceramic charge holder tube and was pushed inside a boron nitride chamber. A voltage between 7 and 9 V was applied to a filament to strike and sustain a plasma. The filament also heated the holder to evaporate the calcium metal. An anode plate with a ~0.2 mm diameter pinhole was used to define the emittance of the beam. A positive voltage was applied to the anode for confinement of the plasma. Calcium ions were extracted from the source and accelerated to an energy of 15 keV and deflected by electrostatic elements in the beam switchyard (refer to Fig. 1.4), into the spectroscopy beam line. Focusing of the ion beam through the beam interaction region was achieved using two sets of quadrupole doublets immediately downstream of the switchyard. The ion

beam current was measured with Faraday cups located in two BOBs: one before and one after the detection region of the spectroscopy beam line. Two collimators, again located in the two BOBs along with the Faraday cups, were used to limit the laser and ion beam sizes to 5 mm and to ensure overlap between the two beams.

Laser System

The Ti:Saph laser was set to 793.21 nm, and this light was frequency doubled to a wavelength of 396.605 nm. A quarter wave plate and polarizer cube were used to restrict the laser power that was coupled into a fiber-optic cable to several mW. The light was transported to the experimental area via fiber-optic cable.

The wavelength values were not centered on the Doppler shifted laser frequency for the D1 line of $^{40}Ca^{+}$ at 15 keV because the present version of the BECOLA DAQ system can only apply positive scanning voltages to the interaction region. To observe the resonance within the voltage range currently accessible to BECOLA, the laser frequency was set to center the resonance at an applied voltage of $\sim$200 V rather than zero.

4.2 Stray Light Characterization

4.2.1 Beam Line Preparation Following Simulation Results

Reducing Reflectivity of Surfaces of Interaction Region

Black aluminum foil was used to cover the reflective surfaces in the photon detection system chamber, and also to fill in gaps where stray light could enter. Locations where the foil was applied are indicated in Fig. 4.2.

The outside of the reflector was not polished, and could serve as an excellent reflector of stray light around the chamber. The outer surfaces of the reflector were covered with black aluminum foil, as shown in Figs. 4.3 and 4.4.

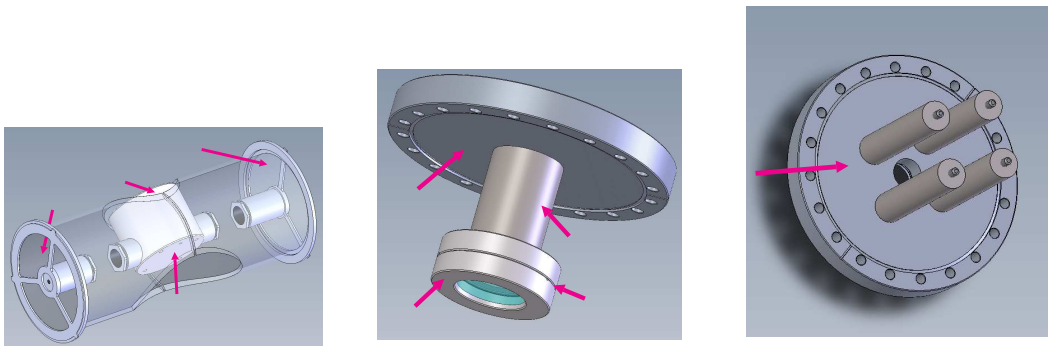

(a) (b) (c)

Figure 4.2: Locations where black aluminum foil was placed to reduce stray light are marked with pink arrows. (a) The reflector outer surfaces and drift tube gaps. (b) The inverted viewport and inverted viewport flange. (c) The reflector flange.

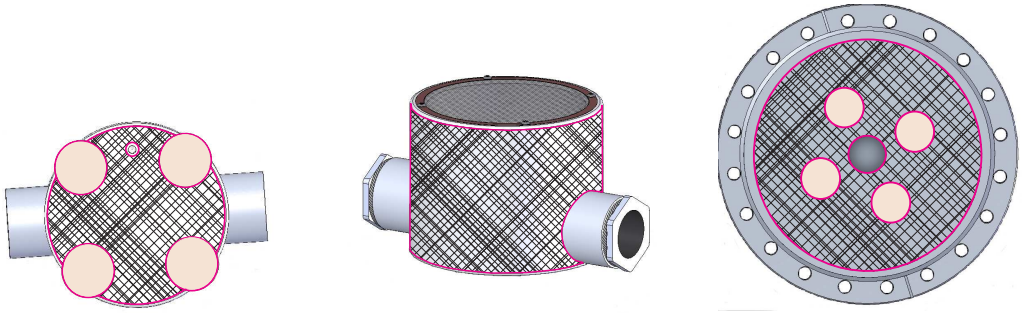

(a) (b) (c)

Figure 4.3: Locations on the (a) Bottom of the reflector; (b) outside of reflector; and (c)reflector flange where black foil was placed to reduce surface reflectance are shown as hatched areas.

The inner ground drift tubes were connected to the outer drift tube to center them in the chamber. The gap between the inner and outer drift tubes is large (∼61-mm long) and stray light could enter the detection chamber via this gap. Black aluminum foil was placed as shown in Fig. 4.5 to cover this gap. In simulations, such coverage of the inner/outer drift tube gap reduced reflected laser light by 90%.

The inverted viewport tube, window flange, 8-inch conflat inverted viewport flange, and 8-inch conflat reflector flange were all fabricated from reflective materials. Each of these components was wrapped with black foil, as shown in Fig. 4.6. In particular, the viewport window flange, by necessity, overlaps the open top of the reflector and

Figure 4.4: Photograph of the ellipsoidal reflector covered in black aluminum foil.

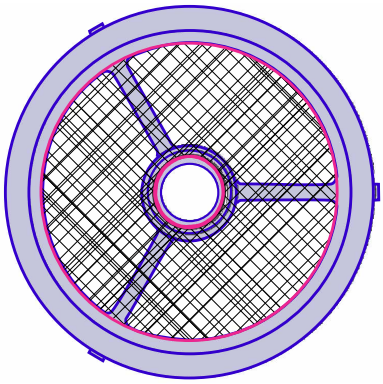

Figure 4.5: The black aluminum foil was placed in the gap between the outer and inner ground drift tubes on both the upstream and downstream sides of the reflector. Crosshatching shows the locations that were covered with black foil to decrease reflectivity.

provides a path for light to scatter back into the reflector. Therefore, it was crucial that the window flange be covered with a non-reflective material (see Fig. 4.7).

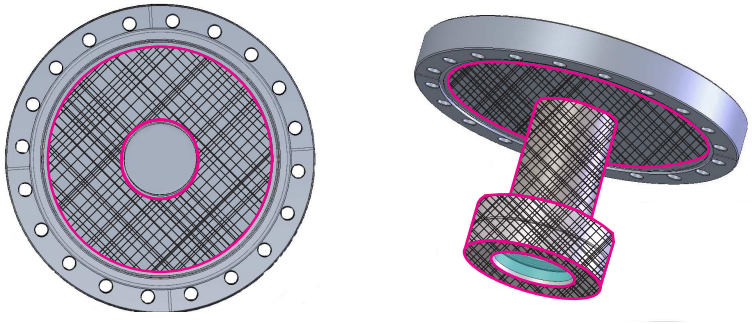

(a) (b)

Figure 4.6: Hatched areas show the locations on the (a) Inverted viewport flange. (b) Inverted viewport tube, window flange, and flange where black foil was placed to reduce surface reflectance.

Figure 4.7: Photograph of the inverted viewport window flange covered in black aluminum foil.

4.3 Commissioning Measurements and Comparison to Simulations

4.3.1 Aperture Configurations

The beam line aperture configurations in the BECOLA interaction region were varied and the S/N measured for comparison with results of the simulations of the S/N from FRED optical engineering software as described in Sec. 3.3.1.

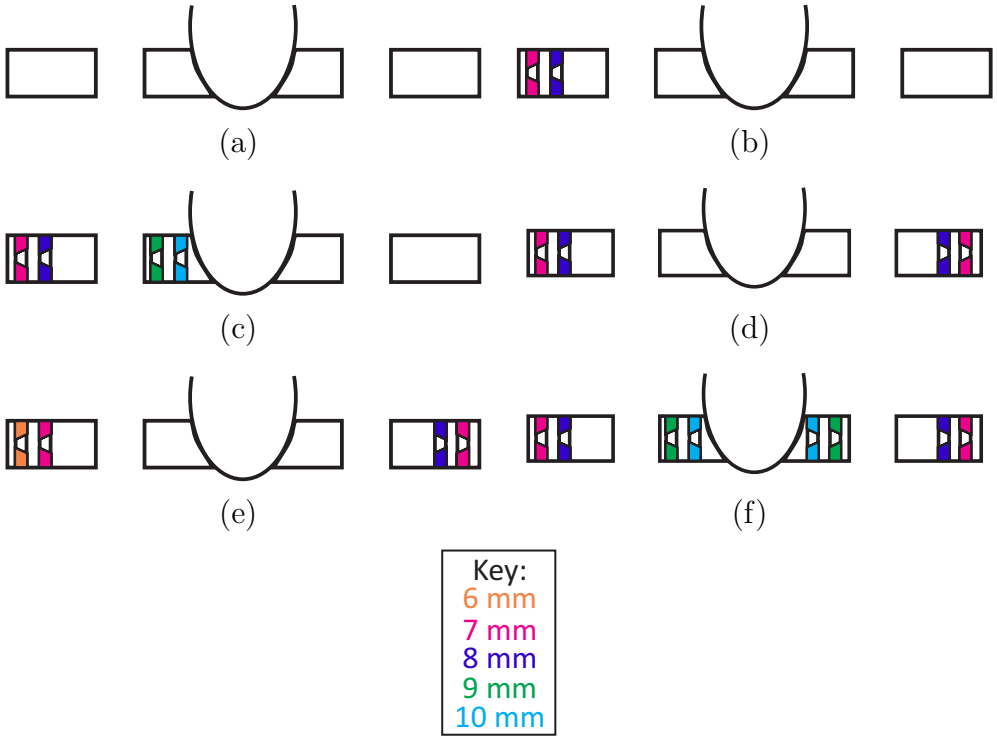

Figure 4.8: Schematic represemtation of the inner drift tube aperture configurations that were tested in BECOLA. (a)-(e) correspond to A-E respectively, (f) is the Mainz system aperture configuration, which was not tested.

The photon detection system had to be vented each time to change the aperture configuration. Caution was taken when changing apertures to ensure that the system geometry (inner and outer drift tube alignment) did not change. As noted in Sec. 3.3.1, the apertures were painted with graphite paint to make them conductive. Although the painting was completed in advance of the measurement, the pieces were

degassed by heating before installation. The beam line aperture measurements were all completed in a one-day period to minimize systematic changes in the laser beam, ion beam and/or beam optics. The laser power and ion beam current were sampled periodically, and used to normalize the observed fluorescence of the $^{40}Ca^{+}$ ions. The results are detailed and discussed in Chapter 5.

4.3.2 PMT Iris Area

The S/N of the blue photon detection system was characterized with various PMT irises placed at the second focal plane. The irises used for commissioning tests included the following: circular irises with diameters of 31.75, 25.4, 19.05, 12.7, and 6.35 mm in diameter, and two rectangular irises of dimension 6.35 $\times$ 25.4 mm, and 6.35 $\times$ 12.7 mm. Recall that the simulation results (Sec. 2.3.2) suggested that the 31.75-mm diameter iris should give the best S/N.

The PMT iris measurements were also all completed in a one-day period. Alignment of the rectangular irises was performed by placing the iris into the inverted viewport and rotating it until it was visually parallel to the beam axis. The PMT was replaced once the iris was aligned. The laser power and ion beam current was sampled periodically and used to normalize the observed fluorescence of the $^{40}Ca^{+}$ ions. The results are contained in the following chapter.

Chapter 5

Results and Discussion

5.1 Line Shape

5.1.1 Typical Resonances

The D1 resonance of $^{40}Ca^{+}$ was used to deduce S/N for the beam aperture and PMT iris measurements outlined in the previous chapter. An example $^{40}Ca^{+}$ fine spectrum collected using the "blue" photon detection system of BECOLA is shown in Fig. 5.1. This spectrum was obtained by limiting the data collection time for a given voltage scan. An oscillation on the isolated main voltage supply was noted early in the BECOLA commissioning, and electronic gates were established to trigger data collection within a limited and consistent period to be "in sync" with the observed AC oscillation (60 Hz), see next section for details.

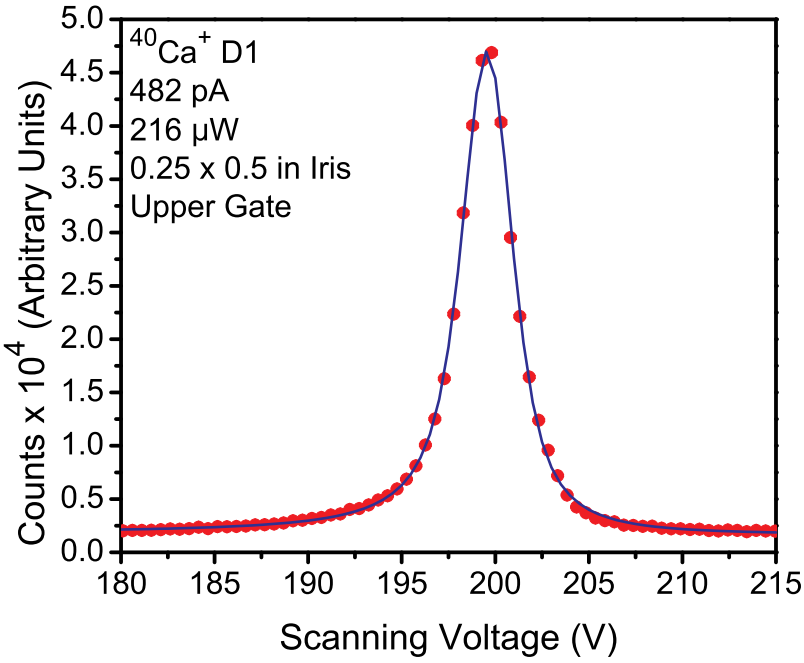

Figure 5.1: Typical $^{40}Ca^{+}$ resonance and fitted curve used to extract S/N ratio for evaluation of photon detection system performance.

Electronic Gates

"D1" fine structure resonance curves for $^{40}Ca^{+}$ collected without discrimination for time are presented in Fig. 5.2. Initial fine structure measurements of $^{40}Ca^{+}$ at BECOLA produced resonance curves with multiple peak structures and unexpectedly large linewidths. The multiple structures were found to vary in intensity and position, as a function of the ion optics.

The suspected cause of the multiple peaks in the Ca^{+} resonance spectrum was a 60 Hz fluctuation in the isolated main AC power for the FUG DC acceleration power supply. The observed oscillation on the 15 kV output voltage of the acceleration power supply is shown in Fig. 5.3. The AC ripple is about 8 V peak to peak. Two of the peaks in the Ca^{+} resonance were believed to correspond to data obtained at the minima and maxima of the ripple. The source of the third peak, most evident in Fig. 5.2(b), remains unknown. An electronic gate was used to restrict the counting

of signals from the PMT to a 500 microsecond region of the oscillation, which had a period of ∼16 ms. Gates were set both on the upper and lower portions of the ripple, as shown in Fig. 5.3. Data were taken for both gate conditions to account for possible differences in S/N due to changes in beam optics.

Implementation of the electronics gates significantly reduced the data collection duty factor. However, use of the gate was necessary to realize a resonance line shape that was more representative of the laser interaction with the ion beam.

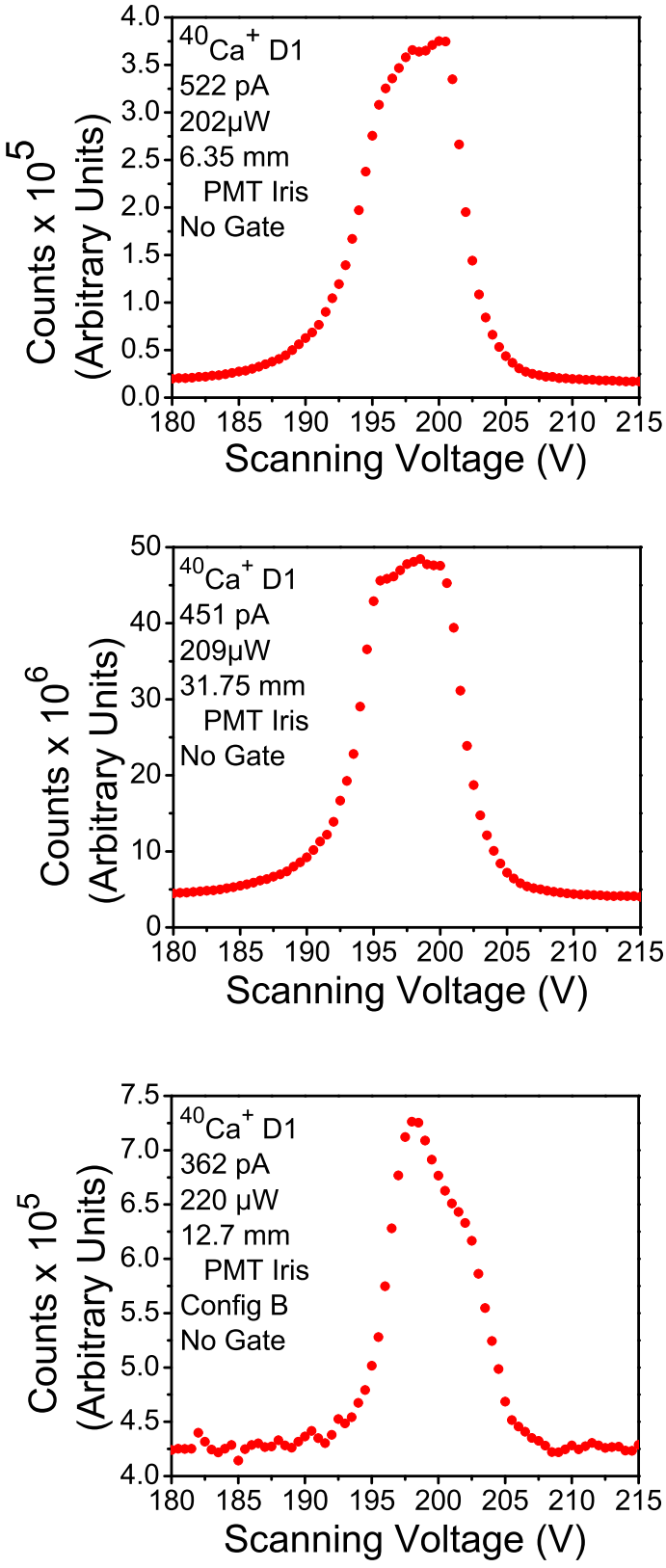

Figure 5.2: Typical $^{40}Ca^{+}$ resonance curves collected with the observed 8 V peak to peak ripple in the FUG DC supply, with no electronic gates. The three figures represent different beam optics settings.

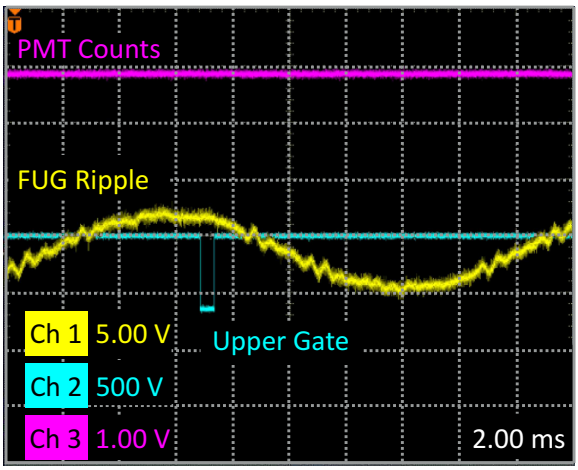

(a) Upper Gate

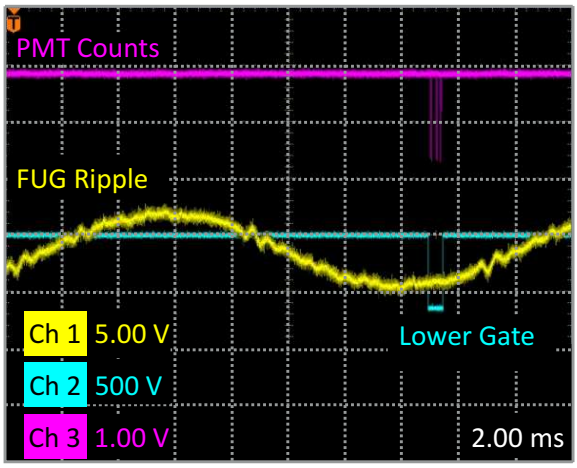

(b) Lower Gate

Figure 5.3: Snapshots of an oscilloscope trace showing the ripple of the FUG power supply. The electronic gates that were applied to reduce the impact of the oscillation on the resonance curves are also shown, as well as the coincidence relationship established by the DAQ for counting PMT signals.

5.1.2 Gated Resonance Spectra

Resonance spectra based on PMT signals that were gated on a limited region of the DC voltage were collected for both the beam line aperture configuration measurement and PMT iris opening measurements. Two distinct resonance structures were observed in the spectra (the secondary structure appearing as a low energy tail). The source of the second resonance peak is still an open question, but may be a property of the plasma conditions inside the ion source.

A typical resonance peak line shape for PMT signals collected using the upper and lower electronic gates are shown in Figs. 5.4 and 5.5, respectively. The resonance line shape is slightly asymmetric with a low-energy component. the line shape was fitted with a Voigt profile that was convoluted with an exponential to phenomologically model the observed low-energy tail.

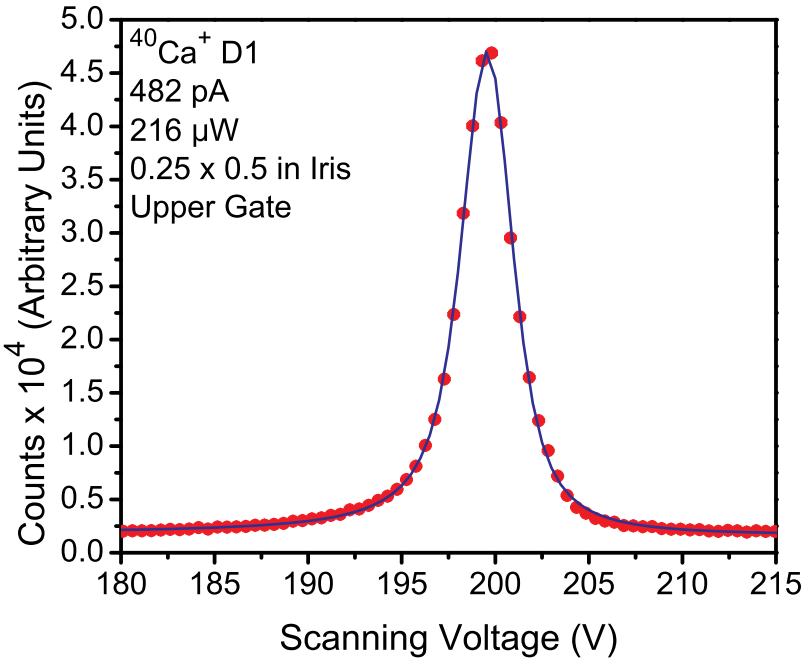

Figure 5.4: Typical $^{40}Ca^{+}$ resonance curve collected with an electronic gate on the upper ripple peak of the 15 kV DC acceleration power supply.

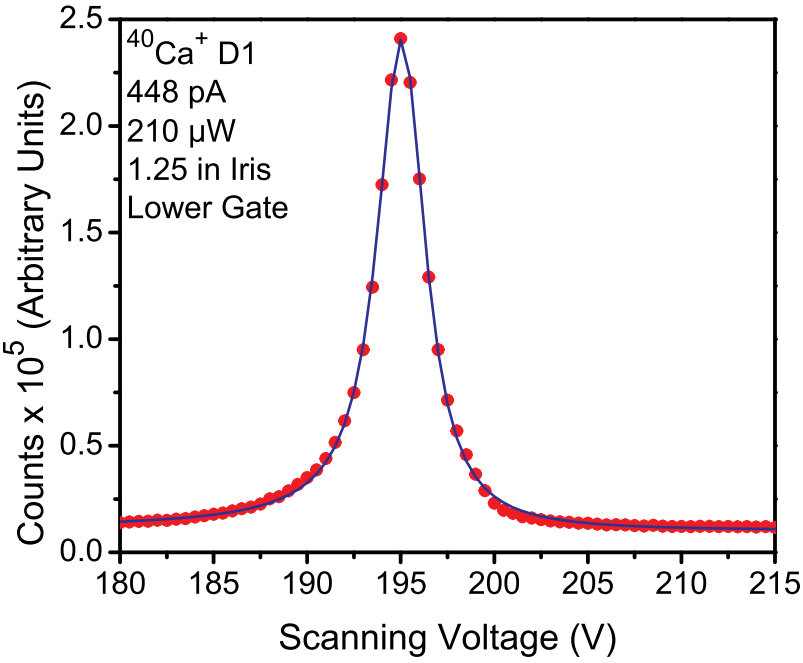

Figure 5.5: Typical $^{40}Ca^{+}$ resonance curve collected with electronic gate on the lower ripple peak.

A more extreme example of the low-energy component of the resonance line shape is shown in Fig. 5.6. The asymmetry of this resonance proved difficult to fit. Various fitting functions tried were: Voigt, Lorentz, Gauss, Voigt*exponential, Voigt + exponential, and multiple Voigt, but none were successful in reproducing the extreme low energy tail. When such an extreme asymmetry was encountered, the line shape was fitted by restricting the fit region to the portion of the line shape well above the tail. Specifically, the low energy asymmetric region between 60% of the peak height and within 1 sigma of the higher energy baseline value was ignored. A single Voigt fit was then applied to the remainder of the high-energy portion of the line shape as depicted in Fig. 5.7.

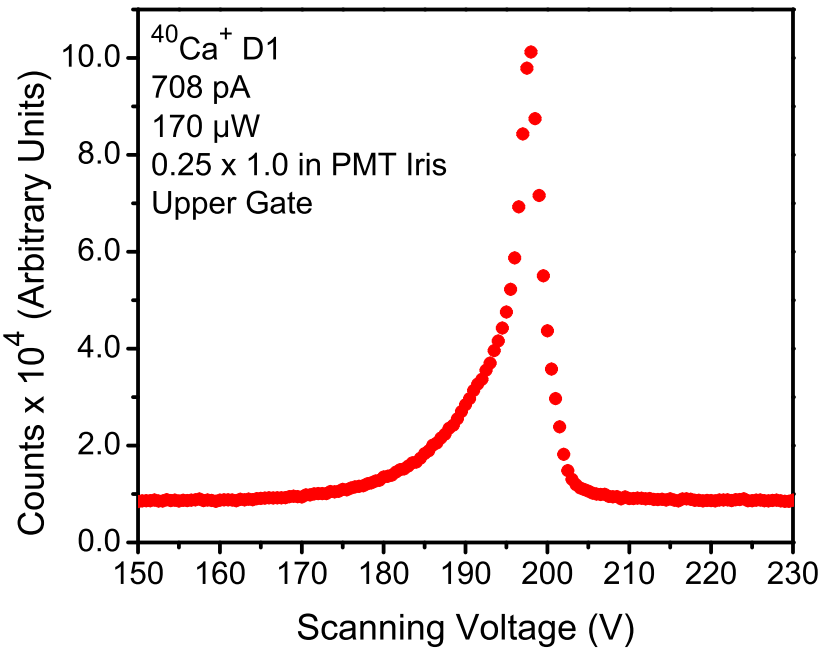

Figure 5.6: Typical $^{40}Ca^{+}$ resonance curves achieved for photon detection system tests with electronic gate on upper ripple peak.

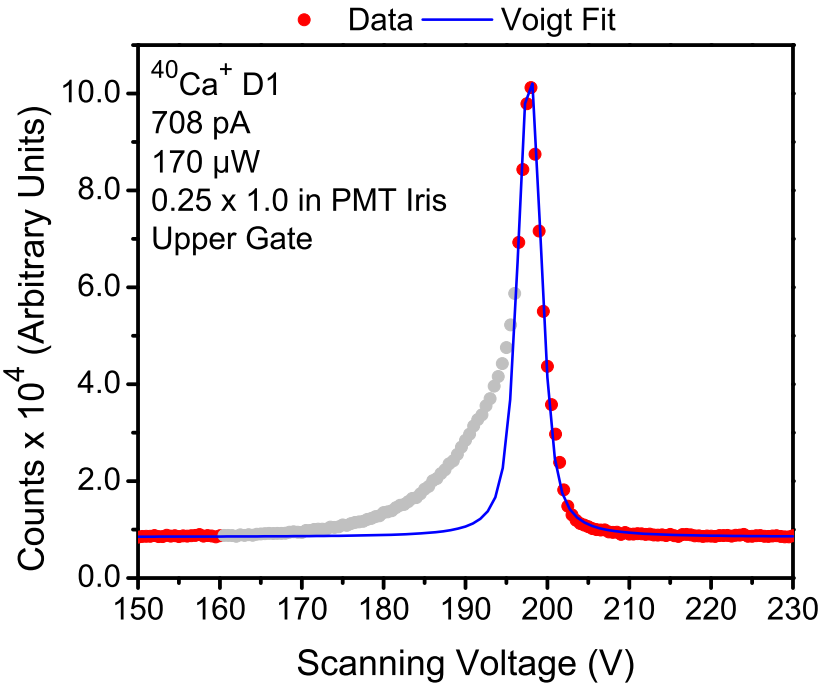

Figure 5.7: Typical $^{40}Ca^{+}$ resonance curves achieved with electronic gate on upper ripple peak with the low-energy tail ignored by the fit. The line is a Voigt profile fit.

5.1.3 S/N Extraction

The S/N was extracted from the resonance spectrum as detailed in Fig. 5.8. The background (B) was the baseline of the resonance, which depended on stray laser light levels. The noise (N) was the fluctuation in the background, and the signal (S) was the amplitude of the resonance peak above the background. The S/N was normalized to both the beam current (I_I) and laser power (I_L) to compare the results of several independent measurements.

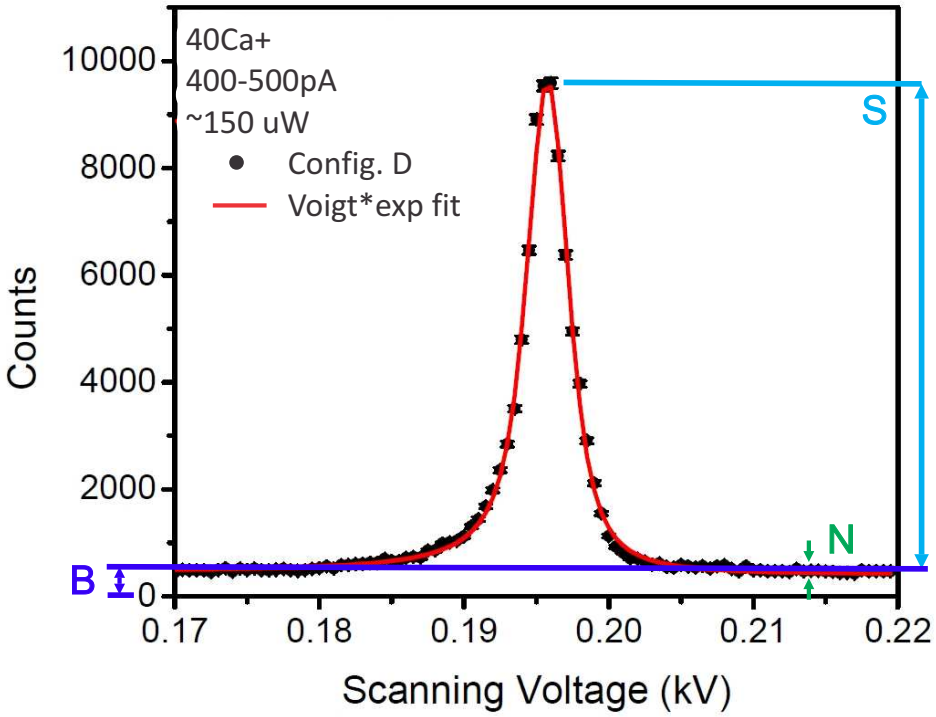

Figure 5.8: S/N extraction from the $^{40}Ca^{+}$ D1 fluorescence peak. Background (B) was defined as the non-resonant counts above zero, the signal (S) was the amplitude of the peak above the background, and the noise (N) was the fluctuation in the background.

S was normalized to give normalized signal (S_N) by:

$$S_N = \frac{S}{I_I I_L}. \tag{5.1}$$

Normalized background (B_N) was similarly obtained as:

$$B_N = \frac{B}{I_I I_L}. \tag{5.2}$$

Normalized noise (N_N) was obtained as:

$$N_N = \frac{N}{\sqrt{I_I I_L}}. \tag{5.3}$$

S/N was obtained from the normalized values as:

$$S/N = \frac{S_N}{N_N}. \tag{5.4}$$

5.2 Beam Line Aperture Configuration Measurements

Five different configurations of the inner drift tube beam line apertures were employed to characterize the S/N response and select an optimum aperture setting for the beam/laser interaction region. Table 5.1 contains the primary data used to deduce S/N. Weighted averages of the relative S/N extracted for each configuration are shown in Fig. 5.9. Recall that the configurations A-C only had apertures upstream of the reflector. Configurations D and E had apertures placed both upstream and downstream of the reflector (refer to Fig. 4.8 for configurations). Placement of apertures downstream of the reflector increased S/N by at least one order of magnitude.

Backscattering of laser light from the end of the beam line, most likely from the laser window, was found to be a significant source of stray light. Black plating of the inner surfaces of the chambers downstream of the photon detection system and placing the laser window at a non-normal angle to the beam are both possible ways to mitigate the scattering of laser light back into the reflector that can be tested in the future.

Table 5.1: Primary data for extraction of S/N as a function of beamline aperture configuration.

	S	δS	B	N	I_I	δI_I	I_L	δI_L	S/N	δS/N
A	31000	9000	49600	100	433	3	212	5	1.1	0.3
A	44000	9000	12930	90	461	2	218.1	0.7	1.6	0.3
B	4200	400	5050	17	330	2	194	1.1	0.91	0.08
B	3600	600	4857	18	395	1.2	187.6	0.6	0.8	0.13
C	12000	3000	12380	40	305.0	0.9	184	2	1.2	0.3
C	10000	2000	13510	11	311.8	0.8	181	1.2	0.8	0.19
D	37000	3000	770	17	413	4	208	1.0	7.4	0.6
D	29000	1300	820	11	376	3	204	4	9.2	0.5
E	22600	700	2220	14	526	4	188	1.8	5.3	0.18
E	23400	610	2640	10	561	3	194	1.8	6.9	0.19

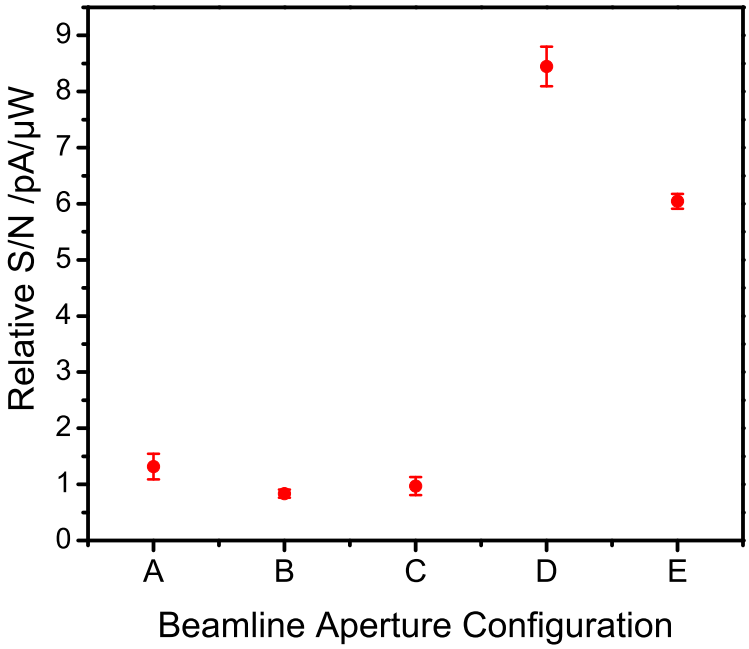

Figure 5.9: Experimental S/N as a function of beam line aperture configuration. S/N is corrected by beam current and laser power.

5.3 PMT Iris Area Measurements

The PMT iris opening area at the second focal plane of the ellipsoidal reflector was varied and relative S/N was deduced from the observed $^{40}Ca^{+}$ resonance curves, again with the goal of optimizing the photon detection system performance. The relative S/N values for the various PMT iris opening areas are presented in Fig. 5.10. The filled circles denote results obtained with circular irises and are labeled by diameters. The S/N results for the rectangular irises are denoted by filled square symbols. The two rectangular iris data points are labeled by the length and width of the rectangular irises, in millimeters, where the longer dimension is along the beam axis. Systematic errors due to laser power fluctuation were not included in the error bars presented in Fig. 5.10.

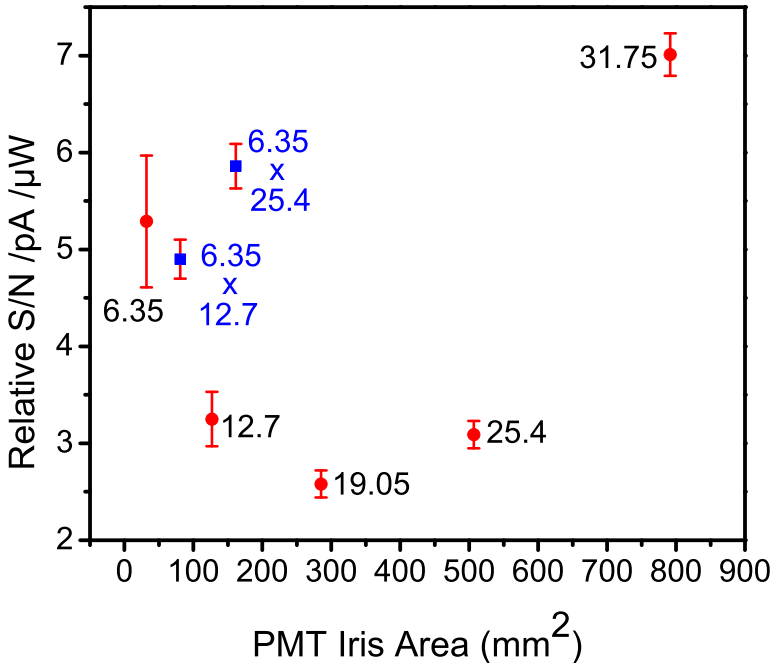

Figure 5.10: Initial experimental S/N as a function of PMT iris area. S/N is corrected by beam current and average laser power.

A second set of measurements with the different irises was completed where the laser power was monitored by splitting the laser beam and monitoring any fluctuations

with a power meter. The average laser power and the one sigma fluctuation in laser power for each run are shown in Fig. 5.11.

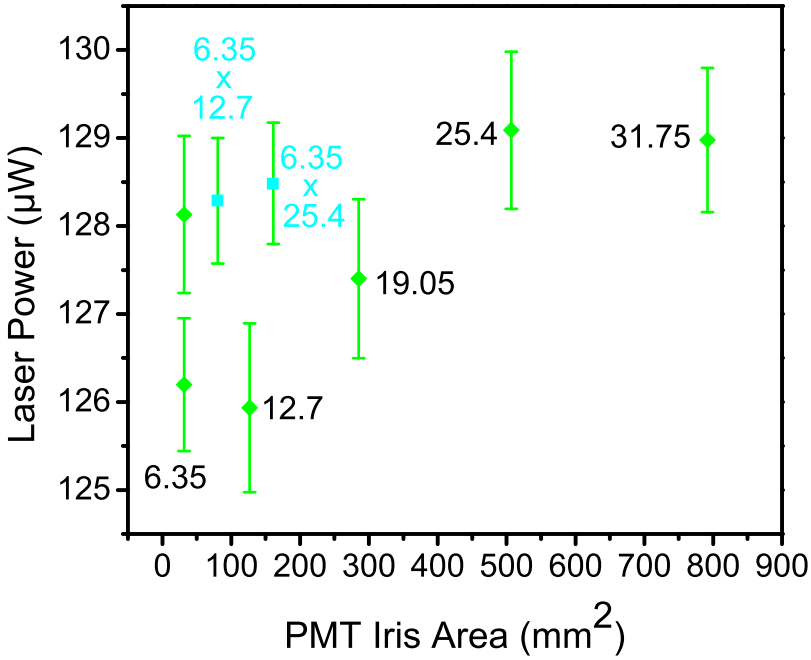

Figure 5.11: Laser power and fluctuation measured during the second run of the PMT iris measurements, note the suppressed zero on vertical scale.

The S/N was deduced for each iris opening using the primary data listed in Table 5.2. The S/N results are shown in Fig. 5.12. The experimental data are presented as in Fig. 5.10, and the simulation results (see Fig.2.4) are denoted by the dashed line. The solid line in Fig. 5.12 is a phenomological fit to the experimental results. The additional normalization of the S/N by the laser power fluctuations reduced the systematic error in the measurements and allowed better comparison of the experimental data to the simulation results.

It was reasoned that the fluorescence light has a distribution that is well focused at the second focal point of the ellipsoidal reflector based on the trends observed in the experimental data. The largest of the PMT iris openings was too small to observe the expected stray light distribution obtained from simulation (see Fig. 2.2) due to constraints introduced by the inverted viewport window. The stray light distribution

Table 5.2: Primary data for extraction of S/N as a function of PMT iris open area.

Iris Area (mm^2)	S	δ S	B	N	I_I	δI_I	I_L	δI_L	S/N	δS/N
31.67	27000	1400	1550	40	1093	4	128.1	0.9	1.9	0.3
31.67	27000	1500	1510	40	1080	10	126.2	0.8	1.9	0.3
80.64	165000	8000	15700	120	1050	5	127.4	0.9	2.7	0.4
126.68	250000	13000	26500	160	990	14	129.1	0.9	3.6	0.5
161.29	249000	13000	33900	180	910	15	129.0	0.8	3.4	0.5
285.02	87000	6000	5750	80	820	14	126	1	3.6	0.4
506.71	64000	3000	5710	80	756	7	128.3	0.7	4.2	0.5
791.73	94000	6000	8580	90	708	5	128.5	0.7	3.9	0.5

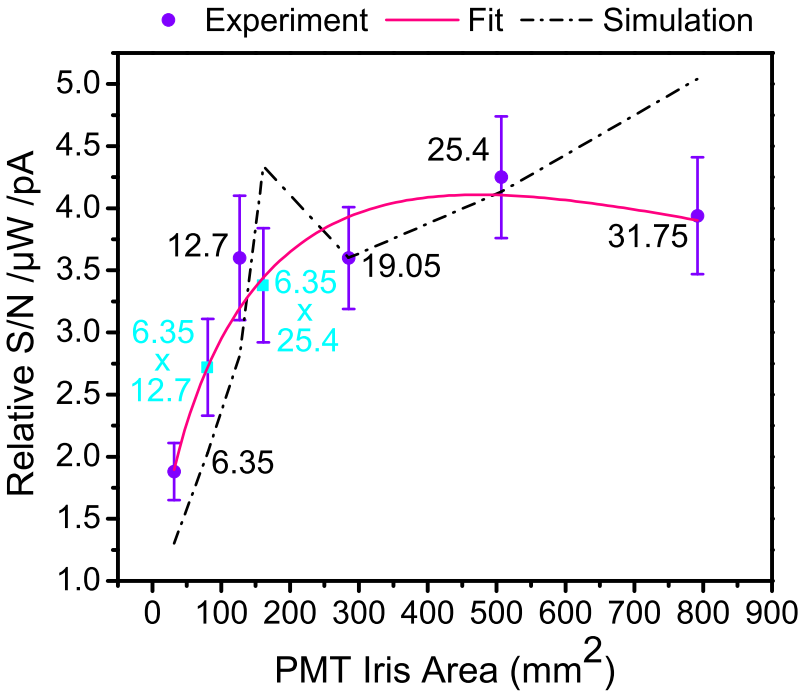

Figure 5.12: Experimental S/N as a function of PMT iris opening area. The S/N was corrected by beam current, laser power and laser power fluctuation.

was assumed to be uniform over the measured second focal plane region. The linear increase in S/N with an increase in the PMT iris opening area due to the drop-off in S/N for larger iris openings after the signal had saturated, and also due to the trend observed in the background levels as a function of PMT iris opening area.

The PMT iris openings with diameters between 12.7 to 31.75 mm gave the same S/N, within the reported error. The function fitted to the data peaks at ∼20 mm for a circular iris opening. Therefore the 19.05 mm diameter circular iris was selected for general use in the "blue" photon detection system. Experimental results matched expectations from simulations.

Chapter 6

Summary and Outlook

A photon detection system was developed to detect fluorescence photons from collinear laser spectroscopy experiments performed at BECOLA. Two systems for "red" and "blue" light were developed based on an initial design from the University of Mainz. The two systems were optimized for use in BECOLA via ray trace simulations. Commissioning measurements of the "blue" system were performed with Ca^+ to verify simulation and optimize sensitivity of the photon detection system.

The $^{40}Ca^+$ D1 resonance lineshape was measured for a variety of beam line aperture configurations and PMT iris openings. S/N ratios were deduced for optimization of the "blue" photon detection system. The optimum beam line aperture configuration was found to be "D" in Fig. 2.5, which had 7 and 8 mm apertures in the inner ground drift tubes both upstream and downstream of the ellipsoidal reflector. The optimum PMT iris opening size was found to be the 19.05 mm diameter circular iris. The "blue" photon detection system, at the optimum setting, has a sensitivity of 1 photon per 128 ions when corrected by the electronics gating time, which corresponds to ion beam rates of about 1×10^5 ions per second.

Commissioning measurements for the "red" photon detection system will be carried out in the near-term with a ^{39}K atomic beam.

BIBLIOGRAPHY

Bibliography

[1] H.-J. Kluge and Wilfried Nörtershäuser. *Spectrochimica Acta B*, **58**:1031, 2003.

[2] L. Weissman et al. *Nucl. Instr. and Meth. Phys. Res. A*, **540**:245, 2005.

[3] K. Minamisono et al. *WSPC Conf. Proc.*, April 2008.

[4] Erst W. Otten. Nuclear radii and moments of unstable isotopes. In *Treatise on Heavy-ion Physics*, volume **8**. Plenum Press, New York, 1987.

[5] K. Shimoda. High-resolution laser spectroscopy. In *Topics in Applied Physics*, volume **13**. Springer-Verlag, Heidelberg, 1976.

[6] Gordon W. F. Drake (Ed.). *Handbook of Atomic, Molecular and Optical Physics*. Springer, New York, 2005.

[7] Christopher J. Foot. *Atomic Physics*. Oxford University Press, New York, 2005.

[8] C. Schwartz. *Phys. Rev.*, **97**(2):380, 1947.

[9] S.L. Kaufman. *Optics Communications*, **17**(3):309, 1976.

[10] William H. Wing et al. *Phys. Rev. Lett.*, **36**(25):1488, 1976.

[11] N. Bendali et al. *J. Phys. B*, **19**:233, 1986.

[12] Colutron research corporation. http://www.colutron.com/products/kit/kit.html.

[13] Ron Fox. Integrating controls and event data. http://docs.nscl.msu.edu/daq/appnotes/Controls.pdf.

[14] Epics. http://www.epics.org/.

[15] Photon engineering. http://www.photonengr.com.

[16] J. Krämer. *Construction and Commissioning of a Collinear Laser Spectroscopy Setup at TRIGA Mainz*. PhD thesis, Johannes Gutenberg-Universität Mainz, 2010.

[17] N.G. Mikhailus. *Zhurnal Priikladnoi Spekrtoskopii*, **11**(3):552, 1969.

[18] M. Hammen. Development, construction and test of an efficient fluorescence detection region for collinear laser spectroscopy at triga-mainz. Master's thesis, Johannes Gutenberg-Universität Mainz, 2010.

[19] Micro-mesh. http://www.sisweb.com/micromesh/.

[20] Mother's power ball mini. http://www.mothers.com/.

[21] Simichrome. http://www.competitionchemicals.com/simichrome/.